Cellular and Molecular Life Sciences (2019) 76:3407–3432
https://doi.org/10.1007/s00018-019-03078-5

Cellular and Molecular Life Sciences

ORIGINAL ARTICLE

# Microglial activation in an amyotrophic lateral sclerosis-like model caused by *Ranbp2* loss and nucleocytoplasmic transport impairment in retinal ganglion neurons

**Kyoung-in Cho[1] · Dosuk Yoon[1] · Minzhong Yu[2,4] · Neal S. Peachey[2,3,4] · Paulo A. Ferreira[1]**

Received: 20 December 2018 / Revised: 21 February 2019 / Accepted: 18 March 2019 / Published online: 3 April 2019


## Abstract

Nucleocytoplasmic transport is dysregulated in sporadic and familial amyotrophic lateral sclerosis (ALS) and retinal ganglion neurons (RGNs) are purportedly involved in ALS. The Ran-binding protein 2 (Ranbp2) controls rate-limiting steps of nucleocytoplasmic transport. Mice with *Ranbp2* loss in Thy1$^+$-motoneurons develop cardinal ALS-like motor traits, but the impairments in RGNs and the degree of dysfunctional consonance between RGNs and motoneurons caused by *Ranbp2* loss are unknown. This will help to understand the role of nucleocytoplasmic transport in the differential vulnerability of neuronal cell types to ALS and to uncover non-motor endophenotypes with pathognomonic signs of ALS. Here, we ascertain Ranbp2's function and endophenotypes in RGNs of an ALS-like mouse model lacking *Ranbp2* in motoneurons and RGNs. Thy1$^+$-RGNs lacking *Ranbp2* shared with motoneurons the dysregulation of nucleocytoplasmic transport. RGN abnormalities were comprised morphologically by soma hypertrophy and optic nerve axonopathy and physiologically by a delay of the visual pathway's evoked potentials. Whole-transcriptome analysis showed restricted transcriptional changes in optic nerves that were distinct from those found in sciatic nerves. Specifically, the level and nucleocytoplasmic partition of the anti-apoptotic and novel substrate of Ranbp2, Pttg1/securin, were dysregulated. Further, acetyl-CoA carboxylase 1, which modulates de novo synthesis of fatty acids and T-cell immunity, showed the highest up-regulation (35-fold). This effect was reflected by the activation of ramified CD11b$^+$ and CD45$^+$-microglia, increase of F4\80$^+$-microglia and a shift from pseudopodial/lamellipodial to amoeboidal F4\80$^+$-microglia intermingled between RGNs of naive mice. Further, there was the intracellular sequestration in RGNs of metalloproteinase-28, which regulates macrophage recruitment and polarization in inflammation. Hence, *Ranbp2* genetic insults in RGNs and motoneurons trigger distinct paracrine signaling likely by the dysregulation of nucleocytoplasmic transport of neuronal-type selective substrates. Immune-modulators underpinning RGN-to-microglial signaling are regulated by Ranbp2, and this neuronal-glial system manifests endophenotypes that are likely useful in the prognosis and diagnosis of motoneuron diseases, such as ALS.

**Keywords** Ran-binding protein 2 (Ranbp2) · Amyotrophic lateral sclerosis (ALS) · Microglia · Nucleocytoplasmic transport · Metalloproteinase-28 (Mmp28) · Acetyl-CoA carboxylase 1 (Acc1) · Retinal ganglion neurons

**Electronic supplementary material** The online version of this article (https://doi.org/10.1007/s00018-019-03078-5) contains supplementary material, which is available to authorized users.

✉ Paulo A. Ferreira
paulo.ferreira@duke.edu

[1] Department of Ophthalmology, Duke University Medical Center, DUEC 3802, 2351 Erwin Road, Durham, NC 27710, USA

[2] Department of Ophthalmic Research, Cole Eye Institute, Cleveland Clinic Foundation, Cleveland, OH 44195, USA

[3] Research Service, Louis Stokes Cleveland Veterans Affairs Medical Center, Cleveland, OH 44106, USA

[4] Department of Ophthalmology, Cleveland Clinic Lerner College of Medicine of Case Western Reserve University, Cleveland, OH 44195, USA

## Introduction

Mounting evidence supports that heterogeneous forms of sporadic and familial ALS share impairments of nucleocytoplasmic transport [1–10] and that these impairments also drive the pathogenesis of other neurodegenerative diseases [10–14]. Changes in nuclear-cytoplasmic distribution of nuclear shuttling substrates are thought to promote proteotoxicity in ALS [7, 8, 10, 15–17]. Parenthetically, substrates of the Ran GTPase cycle act as strong genetic modifiers of the toxicity of ALS substrates [7, 8, 16, 17]. Ran GTPase is a master regulator of nucleocytoplasmic transport by imparting a Ran-GTP to Ran-GDP gradient between the nucleus and cytoplasm. Ran-GTP associates to nuclear export receptors (e.g., exportin-1/CRM1) with their cargoes and to nuclear import receptors (e.g., importin-β) in the nuclear compartment. After exiting the nuclear pore complex (NPC), the disassembly of nuclear export ensembles is achieved by the destabilization and hydrolysis of Ran-GTP from these ensembles [10]. The Ran-binding protein 2 (Ranbp2; also called Nup358) is a unique vertebrate and peripheral nucleoporin, which comprises the cytoplasmic filaments emanating from NPCs [18, 19]. Ranbp2 plays a central role in terminal steps of nuclear export [10]. This is achieved by the docking of exportin-1 ensembles to the zinc-finger cluster domain of Ranbp2 [20–22], by the destabilization of Ran-GTP from nuclear export ensembles that is mediated by the Ran-GTP-binding domains (RBDs) of Ranbp2 [18, 23, 24] and by the recruitment of SUMOylated-Ran GTPase-activating protein-1 (SUMO1-RanGAP1) to Ranbp2 [10, 25–28]. Impairments in Ranbp2 and modular activities thereof promote the dysregulation of nucleocytoplasmic transport of nuclear import and export receptors and the nucleocytoplasmic mislocalization of cell-type selective substrates of Ranbp2 [10, 21, 29–34].

We have shown that conditional loss of *Ranbp2* in Thy1$^{+}$-motoneurons of *SLICK-H::Ranbp2*$^{flox/flox}$ mice causes ALS-like motor traits. These traits consist of rapid declines of motor performance and conduction velocity of sciatic nerve that lead to hind limb paralysis. The motor deficits are followed by respiratory distress and ultimately, death of mice [34]. The changes in motor behaviors are accompanied by the nucleocytoplasmic delocalization in motoneurons of Ran GTPase, exportin-1, importin-β and nuclear shuttling of substrates, such as histone deacetylase 4 (HDAC4) [34]. In addition, differential transcriptome and expression analysis of sciatic nerves and cell bodies of spinal motoneurons between mice with and without *Ranbp2* in motoneurons revealed that loss of *Ranbp2* triggers the dysregulation of neuronal-glial and chemokine signaling without apparent gliosis [34].

Growing evidence indicate that ALS and Ranbp2 affect retinal ganglion neurons (RGNs; a.k.a., retinal ganglion cells). Like in motoneurons, the nuclear envelopes of RGNs are highly enriched in nuclear pores and Ranbp2 [10, 35]. This phenotype appears related to the long-distance burden of transport of cargoes from the nucleus to axons and synapses, a burden which is shared by RGNs and motoneurons [10]. In the inner retina, the peptidyl *cis-trans* prolyl isomerase activity of the cyclophilin domain of Ranbp2 also controls the levels of hnRNPA2B1 [15, 33], a substrate in which mutations cause ALS [36]. Further, motoneurons and RGNs share disease-causing substrates, such as optineurin. Mutations in optineurin cause either ALS [37, 38] or glaucoma, which is the leading blindness disorder caused by the dysfunction and degeneration of RGNs [39, 40]. Parenthetically, a glaucoma-causing mutation in optineurin disrupts its nucleocytoplasmic trafficking [41].

Sporadic and familial forms of ALS (sALS and fALS) appear to produce non-motor syndromic phenotypes in humans. These include changes in the visual evoked potential of the visual pathway from the RGNs to the brain and the thinning of the nerve fiber (axonal) layer of the retina [6, 42–45]. Notably, some of these changes may occur even before clinical motor symptoms ensue. Regardless, the pathogenic drivers shared by motoneurons and RGNs in motoneuron diseases, such as ALS, and the reason(s) for the vulnerability of motoneurons to dysfunction by mutations in ubiquitously expressed genes, are obscure [10, 46]. These barriers also hinder the potential of using RGNs as diagnostic and prognostic tools of motoneuron diseases, such as ALS.

To further the discovery of non-motor and pathognomonic signs of motoneuron disease, such as ALS, herein we ascertain the neuronal-type selective roles of Ranbp2 in Thy1$^{+}$-RGNs in *SLICK-H::Ranbp2*$^{flox/flox}$ mice with ALS-like motor behaviors [34] and that present genetic ablation of *Ranbp2* in both Thy1$^{+}$-motoneurons [34] and RGNs (this study). Loss of *Ranbp2* in Thy1$^{+}$-RGNs promotes axonopathy in the optic nerve, impairment of transmission of visual stimuli from RGNs to the brain and limited changes in the transcriptome of the optic nerve that are distinct from those uncovered in the sciatic nerve [34]. Among these changes, acetyl-CoA carboxylase 1 (*Acc1*) was the most up-regulated mRNA. Acc1 is reported to be at the crux of metabolic shifts and T-cell immunomodulation. In this respect, we found that loss of *Ranbp2* in RGNs caused microglial activation and the intracellular sequestration in somata of RGNs of metalloproteinase 28 (Mmp28), which is also implicated in the control of inflammatory responses. Taken together, these results support that *Ranbp2* loss in RGNs promotes the non-cell autonomous activation of microglia, possibly by

regulating *Acc1* expression and biogenesis and proteostasis of Mmp28.

## Materials and methods

### Mice

The generation of *SLICK-H::Ranbp2*$^{flox/flox}$ with the conditional deletion of *Ranbp2* in motoneurons and RGNs has been described [34]. Briefly, *Thy1-cre/ER*$^{T2}$*-EYFP* (*SLICK-H*) mice with expression of Cre and YFP in Thy1$^{+}$-motoneurons and RGNs [47] were crossed with *Ranbp2*$^{flox/flox}$ [32, 48, 49] to produce *SLICK-H::Ranbp2*$^{flox/flox}$. The generation of transgenic mice expressing wild-type *Ranbp2* tagged with hemagglutinin (HA) in a constitutive *null Ranbp2* background, *Tg-Ranbp2*$^{HA}$*::Ranbp2*$^{-/-}$, and of *Tg-Ranbp2*$^{RBD2/3*-HA}$ mice with mutations in RBD2 and RBD3 of Ranbp2, were previously described [32, 33]. All transgenic lines were on a mixed genetic background and were screened for the lack of *rd1* and *rd8* alleles. Tamoxifen (T5648; Sigma-Aldrich) was administered by oral gavage for 5 consecutive days (0.25 mg/g of body weight) to 4–6-week-old mice as described previously [34]. Mice were reared at < 70 lux and in a pathogen-free transgenic barrier facility at Duke University with 12-h light–dark cycles (6:00 A.M.–6:00 P.M.) under humidity- and temperature-controlled conditions. Mice were given ad libitum access to water and chow diet 5LJ5 (Purina, Saint Louis, MO, USA). Mice of either sex were examined by this study. The Institutional Animal Care and Use Committee of Duke University (A003-14-01) and Cleveland Clinic (2011-0580) approved the mouse protocols and the experiments were performed in accordance with NIH guidelines for the care and use of laboratory animals.

### Fluorescein fundoscopy

Eyes of mice were dilated with a drop of atropine sulfate ophthalmic solution (1%; Alcon Laboratories, Inc., Fort Worth, TX, USA) and then after 5 min with phenylephrine hydrochloride (10%; HUB Pharmaceuticals, LLC, Rancho Cucamonga, CA, USA). To capture images of YFP-labeled RGNs in vivo in mice, non-invasive fundus images were taken with Micron III imaging system (Phoenix Research Laboratories, Pleasanton, CA, USA) in which a Xenon light source is coupled to a CCD-camera coupled microscope with an image resolution of 4 µm in a field of view of 1.8 mm. The pictures were captured in recording mode for 60 s and then the best-focused frames were selected and extracted.

### Visual evoked potential

After overnight dark adaptation mice were anesthetized with ketamine (80 mg/kg) and xylazine (16 mg/kg), and placed on a temperature-regulated heating pad. The pupils were dilated with eyedrops (2.5% phenylephrine HCl, 1% cyclopentolate, 1% tropicamide). VEPs were recorded using an active electrode positioned subcutaneously along the midline of the visual cortex and referenced to a needle electrode placed in the cheek while a third needle electrode was inserted in the tail to serve as the ground lead [33, 50]. VEPs were recorded to achromatic strobe flash stimuli presented in the LKC (Gaithersburg, MD) ganzfeld under dark-adapted conditions. The interstimulus interval ranged from 1.1 to 6 s, increasing with stimulus luminance from − 2.4 to 2.1 log cd s/m$^2$. The amplifier band-pass was set at 1–100 Hz and up to 60 successive responses were averaged to obtain a single VEP waveform. The mouse VEP is dominated by a negative component, N1. The implicit time of the N1 component was measured at the negative peak. The amplitude of the VEP was measured to N1 from the preceding baseline or positive peak (P1).

### Transmission electron microscopy

Mice were anesthetized with ketamine/xylazine (100 mg/kg and 10 mg/kg of body weight, respectively) and then cardiacally perfused with 2.5% glutaraldehyde and 4% paraformaldehyde in 0.1 M sodium cacodylate buffer, pH 7.4. Eyeballs and optic nerves were fixed for 2 h at room temperature followed by 18 h at 4 °C in the same fixative, post-fixed in $OsO_4$, and embedded in Araldite. Ultrathin sections were stained with uranyl acetate and lead citrate. Specimens were examined on a Phillips BioTwin CM120 electron microscope equipped with Gatan Orius and Olympus Morada digital cameras.

### Antibodies

The following and previously characterized antibodies were used for immunofluorescence (IF) or immunoblots (IB): rabbit anti-Ranbp2 (8 µg/ml (IF), Ab-W1W2#10) [33, 34], rabbit anti-hsc70 (1:3000 (IB), ENZO Life Science, Farmingdale, NY, cat# ADI-SPA-816) [34]; mouse mAb414 against nuclear pore complex proteins Nup62, Nup153, and Ranbp2/Nup358 (10 µg/ml (IF), Covance, Emeryville, CA, cat# MMS-120P) [34, 49]; rabbit anti-Ran-GTP (1:100 (IF), gift from Dr. Ian Macara) [34, 51]; rabbit anti-CRM1 (1:50, (IF), Santa Cruz Biotechnology, Santa Cruz, CA, cat# sc-5595) [34]; mouse Ran GTPase (1:100 (IF), BD Biosciences, San Jose, CA, cat# 610341) [34]; mouse anti-importin β (Mab3E9, 1:100, (IF), gift from Dr. Steve Adams) [34, 52]; rabbit anti-HDAC4 (1:500 (IF), Santa Cruz Biotechnology,

cat# sc11418) [34]; rabbit anti-Mmp28 (1:100, (IF), 1:1000 (IB), Proteintech, Rosemont, IL; Cat: 18237-1-AP) [34]; rabbit anti-GFAP (1:200, (IF), DAKO, Carpinteria, CA, cat# z0334) [34, 53]; rat anti- CD11b (1:100, (IF), AbD Serotec, Raleigh, NC, cat# MCA275G) [34, 53]; rat anti-CD45 (1:100, (IF), BD Biosciences (BD Pharmingen), cat# 550239) [53]; rat anti-F4/80 (1:100, (IF), AbD Serotec, cat# MCA9976A); mouse anti-α synuclein (1:100, (IF), Millipore, cat# 36-008-C); goat anti-Brn3 (1:50 (IF), Santa Cruz Biotechnology, cat# sc6026); rabbit anti-Pttg1 (1:100, (IF), 1:1000 (IB), Proteintech, cat# 18040-1-AP); rabbit anti-NR2F2 (1:100 (IF), Abcam) [54]; Alexa Fluor-conjugated secondary antibodies and Hoechst 33 342 were from Invitrogen (Carlsbad, CA).

### TUNEL and EthD-III-cell death assays

Retinal flat mounts were screened for necrosis and apoptosis by incubation of retinal explants with 5 µM EthD-III in Neurobasal2A Medium/B-27 Supplement (Invitrogen) followed by paraformaldehyde (2%) fixation and treatment with the DeadEnd Fluorometric TUNEL System (Promega, Madison) as described [48, 55].

### Immunohistochemistry

Mice were anesthetized with ketamine/xylazine (100 mg/kg and 10 mg/kg of body weight, respectively) followed by cardiac perfusion with 2% paraformaldehyde in 1 × PBS. Eye balls were dissected and incubated with 2% paraformaldehyde in 1 × PBS for 4 h at room temperature. Retinae were dissected and processed for flat mount. Specimens were permeabilized and blocked in 0.5% Triton X-100/5% normal goat serum for 12 h at 4 °C before incubation with primary antibodies for 36–48 h followed by multiple washes with 1 × PBS and incubation for 2 h with anti-goat, anti-rabbit or anti-mouse AlexaFluor-488, AlexaFluor-594 or Cy5-conjugated secondary antibodies. Hoechst (Invitrogen, CA) was used to counter-stain nuclei. Retinal wholemounts were placed on glass slides with retinal ganglion cell layer side up and with Fluoromount-G (Southern Biotech, Birmingham, AL, USA). Images were acquired with a Nikon C1$^+$ laser-scanning confocal microscope coupled with a LU4A4 launching base of four solid state diode lasers (407 nm/100 mW, 488 nm/50 mW, 561 nm/50 mW, and 640 nm/40 mW) and controlled by Nikon EZC1.3.10 software (version 6.4). Pan views of YFP$^+$-RGNs from the marginal to optic nerve head regions of the retina were generated by stitching overlapping field of views of these neurons with Photoshop CS4 or Nikon Elements.

### Morphometric analyses

Quantitation of the numbers of YFP$^+$Thy1$^+$ and Brn3$^+$-RGNs of control (+/+) and −/− mice was performed on images taken from retinal flat mounts (4 image fields of 127 µm$^2$ for both central and peripheral region, 3 mice/genotype). Axon diameters and *g*-ratios were measured and calculated from transmission electron microscopic images of cross-sections of optic nerves. The *g*-ratio of was calculated by the ratio between the averages of the maximal and minimal diameters of the axon and the myelinated fiber using NIKON Elements software AR (ver. 4.0). A minimum of 100 randomly chosen axons per image field from at least 3 non-overlapping images per mouse were used. Quantitative analysis of the number and size of F4/80$^+$-microglia in the ganglion cell layer of the retina was performed by counting and measuring positive immune fluorescence signals in the total image fields of 3 mm$^2$ (approximately a quarter of whole retina was scanned, 3–4 mice/genotype). Surface areas of collapsed confocal stacks of microglia from retinal flat mounts were determined by image thresholding (image segmentation) of calibrated regions of interest (ROI) with Metamorph v7.0 (Molecular Devices).

### Immunoblotting

After mice were killed by cervical dislocation and decapitation, the retinae were carefully dissected and the optic nerves were cut out just before optic chiasma (~ 5 mm). Tissues were snap frozen and placed on dry ice upon collection and stored at − 80 °C. Tissue homogenates were prepared as described previously with minor modifications [33, 48]. Briefly, retinae were homogenized in radioimmune precipitation assay (RIPA) buffer with zirconium oxide beads (Next Advance, Averill Park, NY, USA, ZROB05) and a Bullet blender (Next Advance, BBX24) at 8000 rpm for 3 min, whereas optic nerves were homogenized with stainless beads (Next Advance, SSB02) at 9000 rpm for 2 min with a Bullet blender® (Next Advance, BBX24). Protein concentrations of tissue homogenates were measured by the BCA method using BSA as the standard (Pierce). Equal amounts of homogenates (60 µg of retina homogenates or 30 µg of optic nerve homogenates) were loaded and resolved in 7.5% SDS-PAGE Hoefer or 4–15% gradient Criterion gels (BioRad, Hercules, CA, USA). Blots were also reprobed for hsc70, whose protein levels were unchanged between genotypes, for normalization and quantification of proteins. Unsaturated band intensities were quantified by densitometry with Metamorph v7.0 (Molecular Devices, San Jose, CA, USA), and integrated density values (idv) of bands were normalized to the background and idv of hsc70 as described previously [33, 48].

## Biochemical assays

Retinae and optic nerves were collected immediately after the mice were euthanized, snap frozen and placed on dry ice, and stored at − 80 °C in a freezer. NP-40 extracts were prepared with Bullet blender (Next Advance, BBX24). Free fatty acids (FFA) were measured with the FFA Quantification kit as described [34, 55] and as per manufacturer's instructions (Biovision, Mountain View, CA, USA). A colorimetric assay kit for acetylcholinesterase activity was used as directed per manufacturer (Biovision) and previously described [34]. Data were normalized against protein amounts in NP40-solubilized tissue extracts used for each assay. Protein concentrations of NP40-solubilized extracts were determined by the Bradford assay (BioRad).

## Immunoprecipitation assays

Fresh retinal extracts were solubilized in Nonidet P-40 buffer using Bullet Blender BBX24 (Next Advance Inc.) in the presence of 0.5 mm zirconium oxide beads (Next Advance Inc., Averill Park, NY, USA). 1.2 mg of retinal extracts were pre-cleared with 2 µg of non-immunized IgG (Stressgen, San Diego, CA, USA) and incubated with 50 µl of 50% protein A/G bead slurry (Santa Cruz Biotechnology) at 4 °C for 1 h. The supernatants were incubated with 2 µg of mouse anti-HA antibody (Abcam, Cambridge, MA, USA) at 4 °C for 12 h. Co-immunoprecipitate complexes were resolved by SDS-PAGE in 4–15% gradient Criterion gels (BioRad) and immunoblotted with mouse anti-Pttg1 antibody (Abcam) as described [33, 48].

## Total RNA isolation and RT-qPCR

Total RNA was isolated using TRIzol® (Invitrogen) following manufacturers' guide. RNA was reverse transcribed using SuperScript II First-Strand Synthesis System (Invitrogen). Quantitation of mRNA level with gene-specific primers was carried out with cDNA equivalent to 10 ng of total RNA, SYBR Green PCR Master Mix and ECO Real-Time PCR System (Illumina Inc., San Diego, CA, USA). The data were analyzed using Eco Real-Time PCR System Software version 4.0 (Illumina Inc.). The relative amount of transcripts was calculated by the ΔΔCT method. Data were normalized to GAPDH ($n = 3$–4). Data were analyzed by Student's $t$ test and a $p$ value $\leq 0.05$ was considered significant.

## Deep RNA sequencing by RNA-Seq

The dissections of optic and sciatic nerves were carried out concurrently from the same mice as described [34]. In this study, total RNA from optic nerves was isolated and subjected to deep RNA sequencing exactly as previously described [34]. Briefly, optic nerves were collected and incubated in RNA*later* (Ambion/Thermo Fisher Scientific, Waltham, MA, USA) and snap frozen in liquid nitrogen. Samples were submitted to Otogenetics Corporation (Norcross, GA USA) for RNA-Seq. The Agilent Bioanalyzer or Tapestation and OD260/280 was used to assess the purity and integrity of total RNA. 1–2 µg of cDNA was generated with the Clontech SMARTer cDNA kit (catalog# 634925; Clontech Laboratories, Inc., Mountain View, CA, USA), fragmented with Covaris (Covaris, Inc., Woburn, MA) or Bioruptor (Diagenode, Inc., Denville, NJ, USA), profiled with Agilent Bioanalyzer or Tapestation, and submitted to Illumina library preparation using NEBNext reagents (catalog# E6040; New England Biolabs, Ipswich, MA, USA). The Agilent Bioanalyzer or Tapestation was used to determine the quality, quantity and the size distribution of the Illumina libraries and the libraries were submitted for Illumina HiSeq 2000 or HiSeq 2500 sequencing. Paired-end 100 nucleotide reads were generated from RNA-seq with a sequence depth between 45 and 70 million seq reads and checked for data quality using FASTQC (Babraham Institute, Cambridge, UK). Data were analyzed with DNAnexus (DNAnexus, Inc, Mountain View, CA) or the platform provided by the Center for Biotechnology and Computational Biology (University of Maryland, College Park, MD, USA) [56]. Levels of individual transcripts were expressed as fragments per kilobase of exon per million fragments mapped (FPKM) and were obtained using Cufflinks. A $q$ value less than 0.05 was considered as statistically significant.

## Statistics

Mice were randomly assorted and experiments were performed blind until data analysis. Samples sizes/independent biological replicates were collected (power > 0.8) and these were comparable with other studies using the same mouse lines and genotypes [32, 34, 48]. Two-way repeated measure analyses of variance were used to analyze luminance-response functions for measures of VEP amplitude and timing. $g$-ratios and axonal diameters between groups were assessed with a $t$ test of difference between means using generalized estimating equations (GEE) to account for multiple nerves per mouse. The difference between groups adjusting for axonal diameter was assessed using generalized estimating equations with terms for group, axonal diameter and their interaction (SAS, Cary, NC, USA). The Mann–Whitney test rank-sum test was used to examine areas of perikarya of RGNs. For all other assays, Student's $t$ test for two group comparisons was used. Data are reported as average values ± SD, except otherwise specified. Differences among the groups were considered statistically significant when $p$ value $\leq 0.05$.

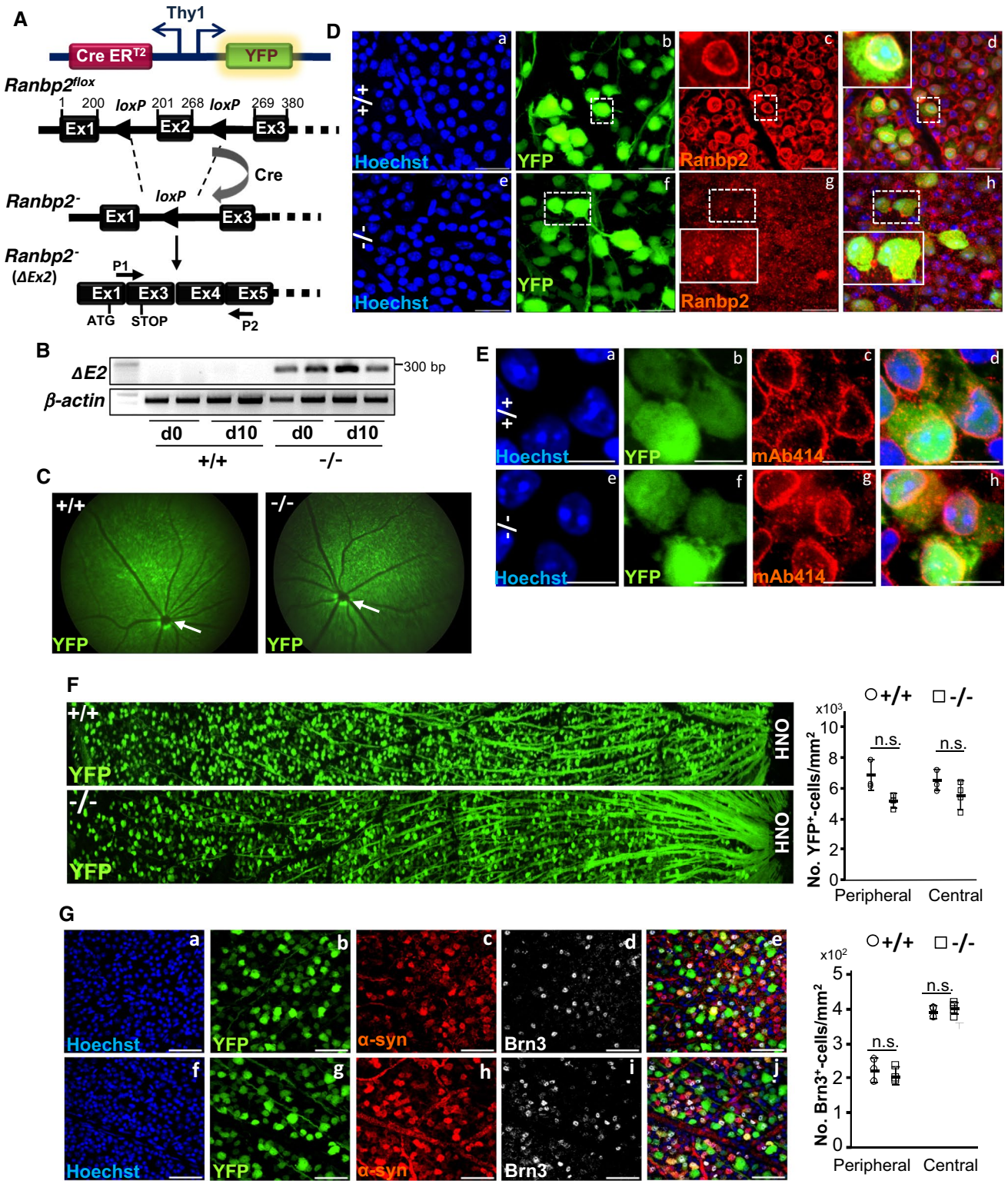
A
Thy1
Cre ER$^{T2}$
YFP
Ranbp2$^{flox}$
1 200 loxP 201 268 loxP 269 380
Ex1 Ex2 Ex3
Cre
loxP
Ranbp2$^{-}$
Ex1 Ex3
Ranbp2$^{-}$
(ΔEx2)
P1
Ex1 Ex3 Ex4 Ex5
ATG STOP
P2
B
ΔE2
β-actin
300 bp
d0 d10 d0 d10
+/+ -/-
C
+/+
-/-
YFP
D
+/+
-/-
Hoechst
YFP
Ranbp2
E
Hoechst
YFP
mAb414
F
ONH
No. YFP$^{+}$-cells/mm$^{2}$
x10$^{3}$
○+/+ □-/-
n.s.
Peripheral Central
G
Hoechst
YFP
α-syn
Brn3
No. Brn3$^{+}$-cells/mm$^{2}$
x10$^{2}$

◂**Fig. 1** Genetic ablation of *Ranbp2* in YFP $^{+}$Thy1$^{+}$-retinal ganglion neurons (RGNs). **A** The single-neuron labeling with inducible Cre-mediated knock-out H transgenic line (SLICK-H) harbors two oppositely oriented *Thy1* promoters that control the co-expression of the yellow fluorescent protein (YFP) and tamoxifen-inducible Cre recombinase (CreER$^{T2}$). This line was used to excise exon 2 (ΔEx2) from a floxed *Ranbp2* gene in mice and generate an out-of-frame exon 3 after splicing of exons 1 and 3. P1 is a hybrid primer against the junction produced by the splicing (fusion) of exons 1 and 3 of the recombinant transcript. P2 is a primer specific for exon 5. **B** Expression of *Ranbp2* mRNA without exon 2 is detected in the retina by RT-PCR with P1 and P2 primers at the end of a daily 5-day regimen of tamoxifen administration, day 0 (d0), and 10 days (d10) after the last dose of tamoxifen. **C** Live fluorescence retinal fundoscopy of dilated pupils of mice showed no overt differences between +/+ and −/− mice at 10 days (d10) after the last dose of tamoxifen. Arrows denote optic nerve head. **D** Confocal images of retinal flat mounts (RGNs facing up) show that compared to +/+ mice (**a**–**d**), YFP$^{+}$-RGNs of −/− mice lack Ranbp2 at the nuclear envelope at d10 (**e**–**h**). Inset picture is an enlarged view of dashed-line box. **E** Confocal images of retinal flat mounts (ganglion neurons facing up) show that the nucleoporins 153 and 62 (Nup153/Nup62) at the nuclear envelope and detected by mAb414 are not affected in YFP$^{+}$-RGNs between +/+ (**a**–**d**) and −/− mice (**e**–**h**) at d10. **F** Low-power confocal images from the optic nerve head (ONH) to the marginal border of the retina (left) and morphometric analyses (right) of retinal flat mounts (ganglion neurons facing up) show that there are no differences of YFP$^{+}$-RGNs between +/+ and −/− mice at d10. Student's *t* test, $n=4$ mice/genotype; data are expressed as mean ± SD. **G** Confocal images (right) and morphometric analyses (left) of retinal flat mounts (ganglion neurons facing up) show that there are no differences in Brn3$^{+}$-RGNs between +/+ and −/− mice at d10. There are also no apparent differences in α-Syn$^{+}$-RGNs between +/+ and −/− mice at d10. Student's *t* test, $n=4$ mice/genotype; data are expressed as mean ± SD. +/+, *SLICK-H::Ranbp2*$^{+/+}$; −/−, *SLICK-H::Ranbp2*$^{flox/flox}$; mAb414, monoclonal Ab414 against Ranbp2(Nup358)/Nup153/Nup62; scale bars 25 µm (**D**), 10 µm (**E**), and 50 µm (**G**); d0 and d10 are days 0 and 10 after the last dose of a daily 5-day regimen of tamoxifen administration, respectively. *α-syn* α-synuclein, *Brn3* Brn3a/b/c POU-domain transcription factors, *OPN* optic nerve head, Ex exon, *n.s.* not significant

## Results

### Mice with targeted *Ranbp2* in Thy1$^{+}$-retinal ganglion neurons (RGNs)

We used the mouse line, single-neuron labeling with inducible Cre-mediated knock-out H transgenic line (*SLICK-H*), which expresses the yellow fluorescent protein (YFP) and tamoxifen-inducible Cre recombinase (CreER$^{T2}$) under the control of neuronal Thy1 promoter in Thy1$^{+}$-motoneurons and RGNs [47, 57–59], to cross with another line harboring a *Ranbp2* floxed gene (*Ranbp2*$^{flox/flox}$) [34, 49]. This cross generated the mouse line, *SLICK-H::Ranbp2*$^{flox/flox}$, which lacks *Ranbp2* in motoneurons and RGNs after tamoxifen administration [34] (Fig. 1A) (unless otherwise noted, hereafter *SLICK-H::Ranbp2*$^{flox/flox}$ (−/−) are mice that underwent tamoxifen treatment). We have previously shown that *SLICK-H::Ranbp2*$^{flox/flox}$ mice with loss of *Ranbp2* in Thy1$^{+}$-motoneurons develop ALS-like motor traits that culminate with the death of mice 10.5 days after a 5-day regimen of tamoxifen [34]. However, the effects of loss of Ranbp2 in Thy1$^{+}$-RGNs are unknown and this was the focus of this study. Like in spinal motoneurons [34], the retina of *SLICK-H::Ranbp2*$^{flox/flox}$ produce a recombinant transcript with a deletion of exon 2, fusion of exons 1 and 3, and premature stop codon in exon 3 as soon as day 0 after a 5-day regimen of tamoxifen (Fig. 1B). The recombinant *Ranbp2* transcript has the translation potential of only the first 31 residues of the 3053 residues that comprise Ranbp2. Fundus fluorescence imaging of eyes of live wild-type and *SLICK-H::Ranbp2*$^{flox/flox}$ mice treated with tamoxifen showed no overt fundoscopic differences of YFP$^{+}$-RGNs and fasciculation of their axons throughout the retina between genotypes on day 10 after the last dose of tamoxifen (d10) (Fig. 1C). In contrast to wild-type mice, confocal microscopy of retinal flat mounts showed that YFP$^{+}$-RGNs lacked Ranbp2 at the nuclear rim at d0 (Fig. 1D). Akin to spinal motoneurons and other studies of other cell types [34, 49], the absence of Ranbp2 did not affect the localization of other nucleoporins at the nuclear rim of YFP$^{+}$-RGNs (e.g., Nup153 and Nup62) (Fig. 1E). Like with motoneurons [34], loss of Ranbp2 did not cause the loss of somata of YFP$^{+}$- and Brn3$^{+}$-RGNs across the retina (Fig. 1F, G). The lack of change in the number of RGNs between genotypes was also confirmed by the complete absence of apoptotic and necrotic RGNs (and other cells) with TUNEL and EthD-III staining of retinal flat mounts.

### *SLICK-H::Ranbp2*$^{flox/flox}$ mice have a delay of implicit times of visual evoked potential (VEP)

We previously found that the sciatic nerves of *SLICK-H::Ranbp2*$^{flox/flox}$ present lower nerve conduction velocity and hind limb paralysis on day 9 after the last dose of tamoxifen [34]. Electrophysiological disturbances in the visual pathway from the RGNs to the primary visual cortex, such as visual evoked potential (VEP) abnormalities, as well as the thinning of the nerve fiber (axonal) layer projected from RGNs were reported in ALS patients [42–45]. To ascertain how loss of *Ranbp2* in YFP$^{+}$-RGNs affected the transmission of luminance stimuli to the visual cortex, we measured the amplitude and latency (implicit times) of VEPs as a function of increasing flash luminance in wild-type and *SLICK-H::Ranbp2*$^{flox/flox}$ mice before and after treatment with tamoxifen [50, 60, 61]. The VEP amplitude reflects the sum input of RGN responses to the visual cortex, whereas the VEP latency reflects the integrity of the transmission of the action potentials by the axons of the optic nerve to the visual cortex [60–62]. As shown in Fig. 2A, there were no overt differences in VEP waveforms between untreated and tamoxifen-treated wild type mice, whereas there were

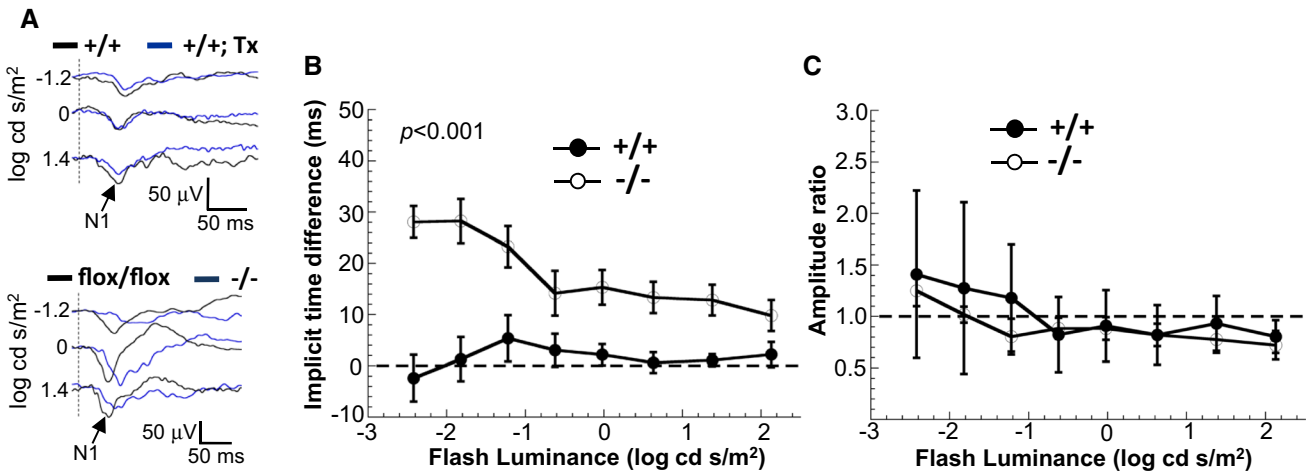


**Fig. 2** Electrophysiological deficits in the visual pathway of *SLICK-H::Ranbp2*$^{flox/flox}$ mice. **A** Visual-evoked potentials (VEPs) recorded to a series of strobe flash stimuli from representative tamoxifen (Tx) untreated (black and baseline tracings) and treated (blue tracings) +/+ (top panel) and *flox/flox* mice (bottom panel). N1, the major negative component of the mouse VEP, is indicated by arrows in the tracings. In comparison to baseline, the VEP obtained following tamoxifen is slower in −/− than +/+ and *flox/flox* mice. The vertical dashed lines indicate the strobe flash stimulus presentation. **B** Average (± sem) difference of VEP implicit times measured at baseline and 5 days (d5) following a daily 5-day regimen of tamoxifen administration for +/+ and −/− mice. In comparison to +/+ controls, two-way repeated measures ANOVAs indicate that VEP implicit times were significantly delayed in −/− mice ($p < 0.001$). **C** Average (± sem) difference of VEP amplitude measured at baseline and 5 days (d5) following a daily 5-day regimen of tamoxifen administration for +/+ and −/− mice. Two-way repeated measures ANOVAs indicate that VEP amplitude was not significantly affected between genotypes ($p > 0.05$). $n = 6$ mice/genotype. +/+ *SLICK-H::Ranbp2*$^{+/+}$, −/− *SLICK-H::Ranbp2*$^{flox/flox}$, *flox/flox* tamoxifen-untreated *SLICK-H::Ranbp2*$^{flox/flox}$

noticeable changes in the implicit time of the dominant negative wave component (N1) of the VEP waveforms to strobe flash stimuli between untreated and tamoxifen-treated *SLICK-H::Ranbp2*$^{flox/flox}$ mice on day 5 (d5) after the last dose of tamoxifen. Luminance-response functions for the N1 implicit time and amplitude of VEPs showed that there was a significant delay in the N1 implicit time of tamoxifen-treated *SLICK-H::Ranbp2*$^{flox/flox}$ compared to wild-type mice ($p < 0.001$; Fig. 2B), while the amplitudes of VEPs did not differ between genotypes (Fig. 2C).

## RGNs and optic nerves of *SLICK-H::Ranbp2*$^{flox/flox}$ mice develop morphometric abnormalities

To gain further insights into the bases of the impairment of VEPs in *SLICK-H::Ranbp2*$^{flox/flox}$ mice, we compared morphometric analyses of myelinated axons and cell bodies of RGNs between genotypes. Examination of transmission electron microscopy images of RGNs between untreated and tamoxifen-treated *SLICK-H::Ranbp2*$^{flox/flox}$ mice found no overt differences in the ultrastructural morphology of the somata of these neurons at d10 (Fig. 3A). However, morphometric analyses showed a significant increase of the mean perikarya area (hypertrophy) of YFP$^{+}$-RGNs of *SLICK-H::Ranbp2*$^{flox/flox}$ mice compared to *SLICK-H::Ranbp2*$^{+/+}$ by d10 ($p = 0.00005$) (Fig. 3B). Next, we examined ultrathin sections of the optic nerve at d10 and found that there were also no overt differences in morphology of myelinated axons of the optic nerve between genotypes (Fig. 3C).

To uncover potential changes in myelination and axonal diameters of the fibers of the optic nerve, we measured the *g*-ratio and axonal diameters. The *g*-ratio quantifies changes in the ratio between the diameter of the inner axon alone and that of the axon with myelin sheath. We found that by d10 the *g*-ratio were slightly but significantly diminished between *SLICK-H::Ranbp2*$^{flox/flox}$ and *SLICK-H::Ranbp2*$^{+/+}$ ($p = 0.001$), whereas the diameters of axons of the optic nerve were strongly decreased by ~ 40% in *SLICK-H::Ranbp2*$^{flox/flox}$ compared *SLICK-H::Ranbp2*$^{+/+}$ ($p = 0.001$) (Fig. 3D). A decrease in *g*-ratio typically indicates hypermyelination, but a decrease of axonal caliber alone also contributes to a decline in *g*-ratio [63]. Hence, we built scatter plots of *g*-ratios of axons of optic nerve as a function of the axonal diameter to examine further relationships between *g*-ratio and axon caliber of the optic nerve (Fig. 3E). This analysis showed that compared to *SLICK-H::Ranbp2*$^{+/+}$, there was a significant leftward shift in the scatter plot of *SLICK-H::Ranbp2*$^{flox/flox}$ mice indicating that large caliber axons were affected by a strong decrease in axon diameter (Fig. 3E). This observation was also supported by the examination of the slopes of the regression lines (0.0269 ± 0.033 vs 0.0385 ± 0.0006) that diverged with the increase of axon caliber and that were significantly different between genotypes ($p = 0.0006$) (Fig. 3E). Likewise,

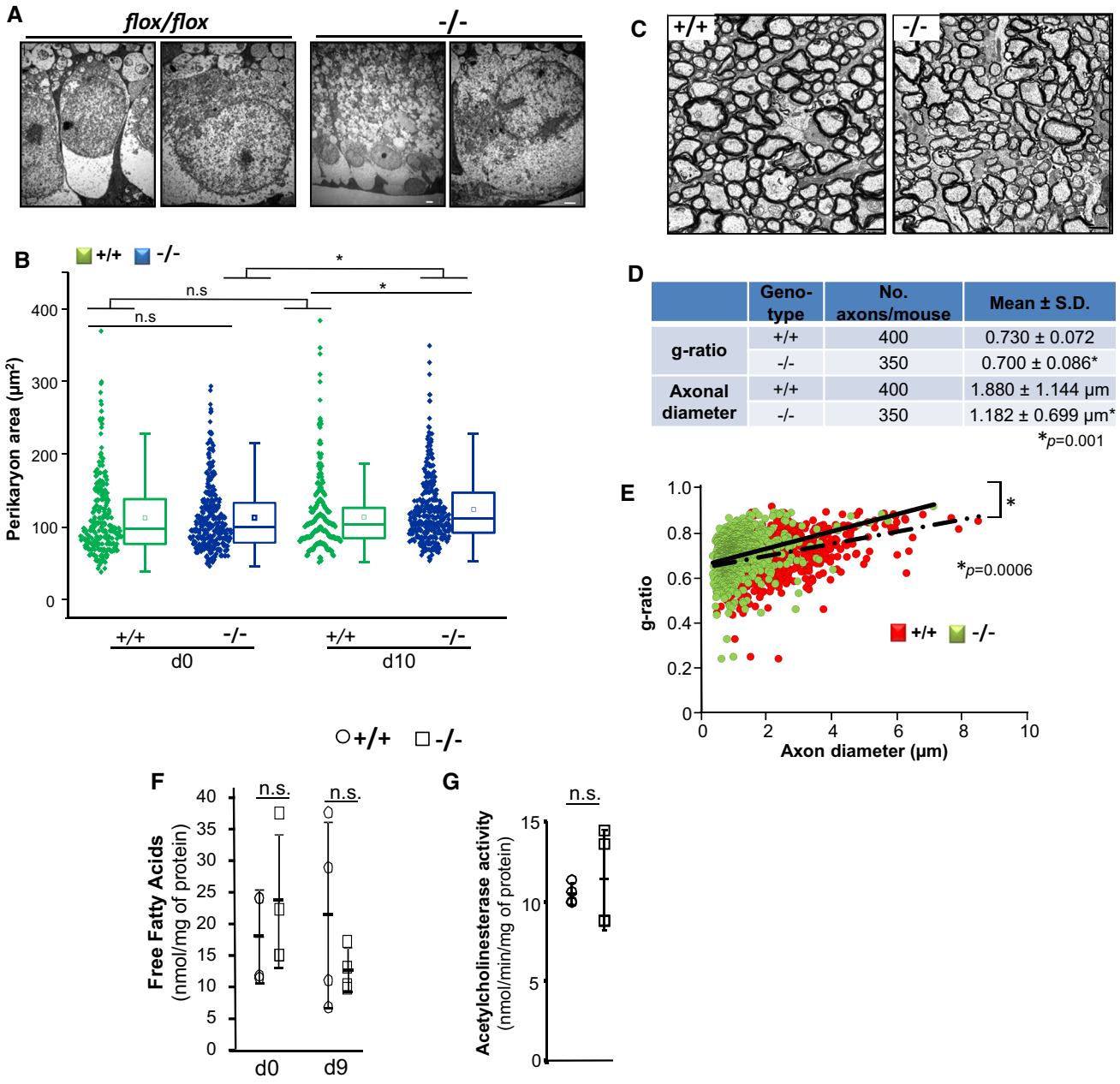


| | Geno-type | No. axons/mouse | Mean ± S.D. |
|---|---|---|---|
| g-ratio | +/+ | 400 | 0.730 ± 0.072 |
| | -/- | 350 | 0.700 ± 0.086* |
| Axonal diameter | +/+ | 400 | 1.880 ± 1.144 µm |
| | -/- | 350 | 1.182 ± 0.699 µm* |

*$p$=0.001

**Fig. 3** Morphometric and lipid profile changes of retinal ganglion neurons (RGNs) of *SLICK-H::Ranbp2*$^{flox/flox}$ mice. **A** Representative low (left) and high power (right) transmission electron micrographs of RGNs of the retina of *flox/flox* (without tamoxifen treatment) and −/− mice at day 10 (d10) post-tamoxifen administration. No overt ultrastructural changes in somata of RGNs were observed between tamoxifen-treated and untreated mice. **B** Dot-box plots of non-parametric analyses of perikarya (soma) area of YFP$^{+}$-RGNs. The perikarya of YFP$^{+}$-RGNs of −/− mice develop hypertrophy. Box-plot edges denote the 25th and 75th percentiles of the data, and the centerline denotes the median value. $n$ = 291(+/+, d0), 340 (+/+, d10), 332 (−/−, d0), 335 (−/−, d10); *$p \leq 0.00005$, Mann–Whitney test, $n$ = 4 mice/genotype. **C** Representative cross-sections of transmission electron micrographs of myelinated optic nerves of +/+ and −/− mice at d10. **D** Measurements of *g*-ratios and axonal diameters of optic nerves showed significant decreases between genotypes. Data are expressed as mean ± SD, *$p < 0.001$, *t* tests with GEE, $n$ = 4 mice/genotype. **E** Scatter plots between *g*-ratios and axonal diameter of fibers of optic nerves. Slopes of +/+ and −/− mice are 0.0269 ± 0.033 and 0.0385 ± 0.0006, respectively; *$p < 0.0006$ (interaction term), *t* tests with GEE, $n$ = 4 mice/genotype. Slope values are expressed as mean ± s.e.m. Slopes diverged with the increase of axon caliber. **F** The levels of free fatty acids are unchanged between gentotypes in the optic nerve at d9 (Student's *t* test, $n$ = 4 mice/genotype). Data are expressed as mean ± SD. **G** Acetylcholinesterase activity is unaltered between genotypes in the visual cortex at d9 (Student's *t* test, $n$ = 4 mice/genotype). Scale bars 2 µm (**A**, **C**). *n.s.* non-significant, −/− *SLICK-H::Ranbp2*$^{flox/flox}$, +/+ *SLICK-H::Ranbp2*$^{+/+}$, d0, d9 and d10 days 0, 9 and 10 post-tamoxifen administration, respectively

the slope for each genotype and optic nerve was significant ($p < 0.0001$). Collectively, these data indicate that large caliber axons of *SLICK-H::Ranbp2*$^{flox/flox}$ mice exhibit an increased vulnerability to degeneration as reflected by a selective and major decrease of axonal diameter of high caliber fibers and that these effects were accompanied by the hypertrophy of somata of YFP$^+$-RGNs of *SLICK-H::Ranbp2*$^{flox/flox}$ mice.

We have previously found that the levels of free fatty acids (FFA) were decreased in the sciatic nerve of *SLICK-H::Ranbp2*$^{flox/flox}$ mice [34]. Hence, we also examined the levels of free fatty acids in the optic nerve between genotypes. We found that the levels of FFA (octanoate and longer fatty acids) remained unchanged between genotypes (Fig. 3F). Finally, we examined the levels of acetylcholinesterase (AChE) activity in the visual cortex, since cholinergic synapses of motoneurons may be affected during the course of some forms of ALS and acetylcholine (ACh) modulates the processing of visual information in the visual cortex (V1) [64]. However, and like in spinal motoneurons [34], the activity of AChE was similar in the visual cortex between genotypes at d9 (Fig. 3G).

## RGNs of *SLICK-H::Ranbp2*$^{flox/flox}$ mice present impairments in the nuclear-cytoplasmic distribution of direct and accessory partners of Ranbp2

Ranbp2 is a large modular protein, whose domains interact with specific partners that mediate nucleocytoplasmic transport (Fig. 4A) [10]. In particular, the Ran-binding domains (RBDs) of Ranbp2 associate with Ran-GTP and the accessory nuclear import receptor, importin-β [10, 23, 24], whereas the zinc-finger (ZnF)-cluster domain is a docking site for the nuclear export receptor, exportin-1 (Fig. 4A) [10, 20]. Hence, loss of *Ranbp2* was shown to promote the nucleocytoplasmic mislocalization of these receptors, Ran GTPase and accessory substrates in spinal motoneurons and other cell types [10, 32–34]. Further, we have shown that the orphan nuclear receptor, NR2F2, interacts with Ranbp2 in the retina [54]. In addition, HDAC4 is a substrate of Ranbp2 [65] and Ranbp2 controls the nucleocytoplasmic distribution of HDAC4 in spinal motoneurons [34] and its proteostasis via the ubiquitin proteasome system (UPS) [66]. Akin to these findings, we also found that the nucleocytoplasmic localizations of these direct and accessory partners of Ranbp2 were affected by loss of Ranbp2 in RGNs (Fig. 4B–D). We found that importin-β and exportin-1 were localized at the nuclear rim and intranuclear compartment of YFP$^+$-RGNs of wild-type mice, whereas there was strong accumulation of importin-β and exportin-1 in the cytoplasmic compartment of YFP$^+$- RGNs of *SLICK-H::Ranbp2*$^{flox/flox}$ (Fig. 4B). These effects were also accompanied by the general decrease of NR2F2$^+$-nuclei of YFP$^+$-RGNs of *SLICK-H::Ranbp2*$^{flox/flox}$ compared to wild type mice (Fig. 4C). Like in spinal motoneurons [34], HDAC4 was largely excluded from the nuclear compartment of YFP$^+$-RGNs of wild type mice, but this subcellular compartmentalization was lost in *SLICK-H::Ranbp2*$^{flox/flox}$ (Fig. 4C). Ran GTPase and its nucleotide-bound form, Ran-GTP, were found diffusely dispersed throughout the perikarya and nuclei of YFP$^+$-RGNs of wild type mice (Fig. 4D), but Ran-GTP was also found at the nuclear rim of YFP$^+$-RGNs (Fig. 4D, a"'). In contrast, Ran GTPase localization appeared redistributed mostly to the cytosolic compartment, and Ran-GTP localization in the nucleus and at the nuclear rim was largely lost in YFP$^+$-RGNs of *SLICK-H::Ranbp2*$^{flox/flox}$ (Fig. 4D).

## Differential transcriptomics and gene expression analysis of optic nerves between wild-type and *SLICK-H::Ranbp2*$^{flox/flox}$

Our prior differential transcriptome and gene expression studies of sciatic nerves between wild-type and *SLICK-H::Ranbp2*$^{flox/flox}$ mice uncovered the regulation of 25 transcripts by Ranbp2 including a set of chemokine ligands [34]. To gain insights into transcriptome changes that underpin the pathobiological phenotypes shared by or unique to sciatic and optic nerves after nucleocytoplasmic impairment caused by loss of *Ranbp2*, we performed differential and whole transcriptome analysis between genotypes of optic nerves that are comprised largely of axons of RGNs and oligodendrocytes (myelin sheaths). Transcriptome analysis was carried out by deep RNA sequencing (RNA-seq) of 45–70 million total seq reads of *SLICK-H::Ranbp2*$^{+/+}$, *SLICK-H::Ranbp2*$^{flox/flox}$ and *Tg-Ranbp2*$^{RBD2/3*-HA}$::*SLICK-H::Ranbp2*$^{flox/flox}$ (Fig. 5A). The *Tg-Ranbp2*$^{RBD2/3*-HA}$::*SLICK-H::Ranbp2*$^{flox/flox}$ expresses a BAC transgene with mutations in RBD2 and RBD3 of Ranbp2 in a *null Ranbp2* background and that abolish their association to Ran-GTP and importin-β [32, 34]. This line served as an additional control, because expression of *Tg-Ranbp2*$^{RBD2/3*-HA}$ rescues the lethality and motor behaviors of *SLICK-H::Ranbp2*$^{flox/flox}$ and thereby serves to filter out compensatory transcriptional responses lacking pathophysiological relevance [32, 34].

To identify transcripts differentially modulated between genotypes at d10, we applied a cut-off with a $\log_2$ fold-change (FC) $\geq |4|$ and a false discovery rate (FDR) $< 0.05$ ($q < 0.05$) for the whole transcriptome analysis. As shown in Fig. 5A, the differential transcriptome analysis identified 50 and 13 transcripts that were differentially up-regulated and down-regulated, respectively, between optic nerves of wild-type and *SLICK-H::Ranbp2*$^{flox/flox}$ (Fig. 5A). Then, we independently validated the relative magnitude, direction

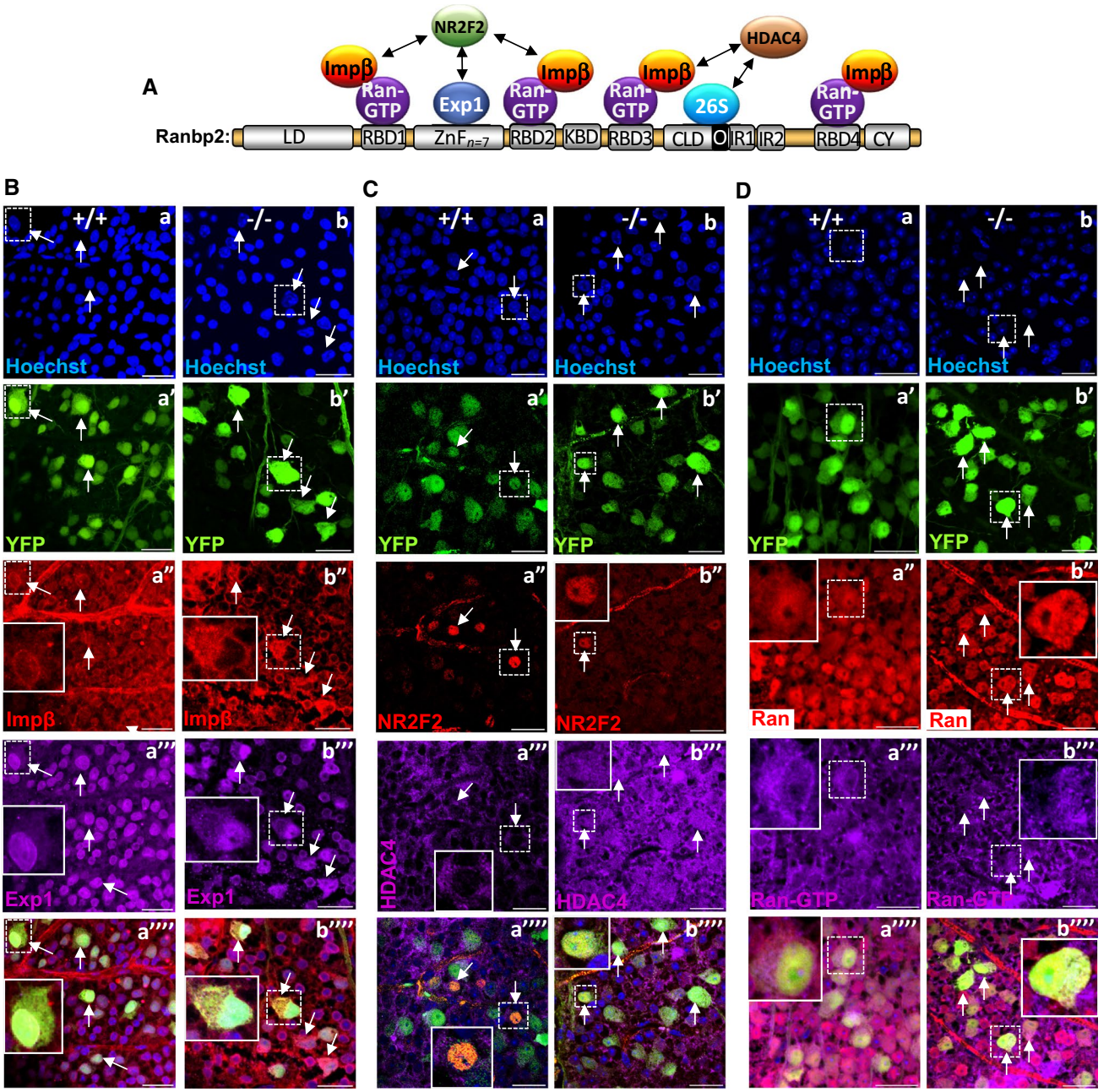


**Fig. 4** Disruption of subcellular localization of partners and substrates of Ranbp2 in retinal ganglion neurons (RGNs) of *SLICK-H::Ranbp2*$^{flox/flox}$ mice. **A** Schematic diagram of the multimodular structure of Ranbp2 and its partners. **B**–**D** Confocal images of RGNs of retinal flat mounts (ganglion neurons facing up) at d10 (day10) post-tamoxifen administration and co-immunostained with partners and substrates of Ranbp2. Inset pictures are enlarged views of dashed-line boxes. **B** Importin-β (**a″**) and exportin-1 (**a‴**) localize to the nuclear rim and nucleus of YFP$^{+}$-RGNs of +/+ mice (arrows). In −/− mice, YFP$^{+}$-RGNs have cytosolic accumulation of importin-β (**b″**), and cytosolic and intranuclear accumulation of exportin-1 (**b‴**) (arrows). **C** NR2F2 (**a″**) localizes to nuclei, whereas HDAC4 (**a‴**) is excluded from the nuclei compartment of YFP$^{+}$-RGNs of +/+ mice. In −/− mice, there is loss of NR2F2$^{+}$-RGNs (**b″**) and of the subcellular partitioning of HDAC4 in YFP$^{+}$-RGNs (**b‴**). **D** Ran GTPase (**a″**) and Ran-GTP (**a‴**) localize diffusely throughout the cytosolic and nuclear compartments of YFP$^{+}$-RGNs of +/+ mice and Ran-GTP localizes also to the nuclear rims of YFP$^{+}$-RGNs (**a‴**). In −/− mice, there is subcellular redistribution of Ran GTPase (**b″**) and Ran-GTP (**b‴**) into the cytosolic compartment and loss of Ran-GTP at the nuclear rims of YFP$^{+}$-RGNs. Scale bars 25 µm. *LD* leucine-rich domain, *RBD*$_{n=1-4}$ Ran GTPase-binding domains, $n=1$–4, *ZnF*$_{n=7}$ zinc finger-cluster domain, *KBD* kinesin-1-binding domain, *CLD* cyclophilin-like domain, *IR1 and IR2* internal repeats 1 and 2, respectively, *O* overlapping region between CLD and IR1, *CY* cyclophilin domain, *Exp1* exportin-1, *impβ* importin-β, *HDAC4* histone deacetylase 4, *Ran* Ran GTPase, *26S* subunits of the 26S proteasome, *NR2F2* nuclear receptor 2 factor 2, −/− *SLICK-H::Ranbp2*$^{flox/flox}$, +/+ *SLICK-H::Ranbp2*$^{+/+}$

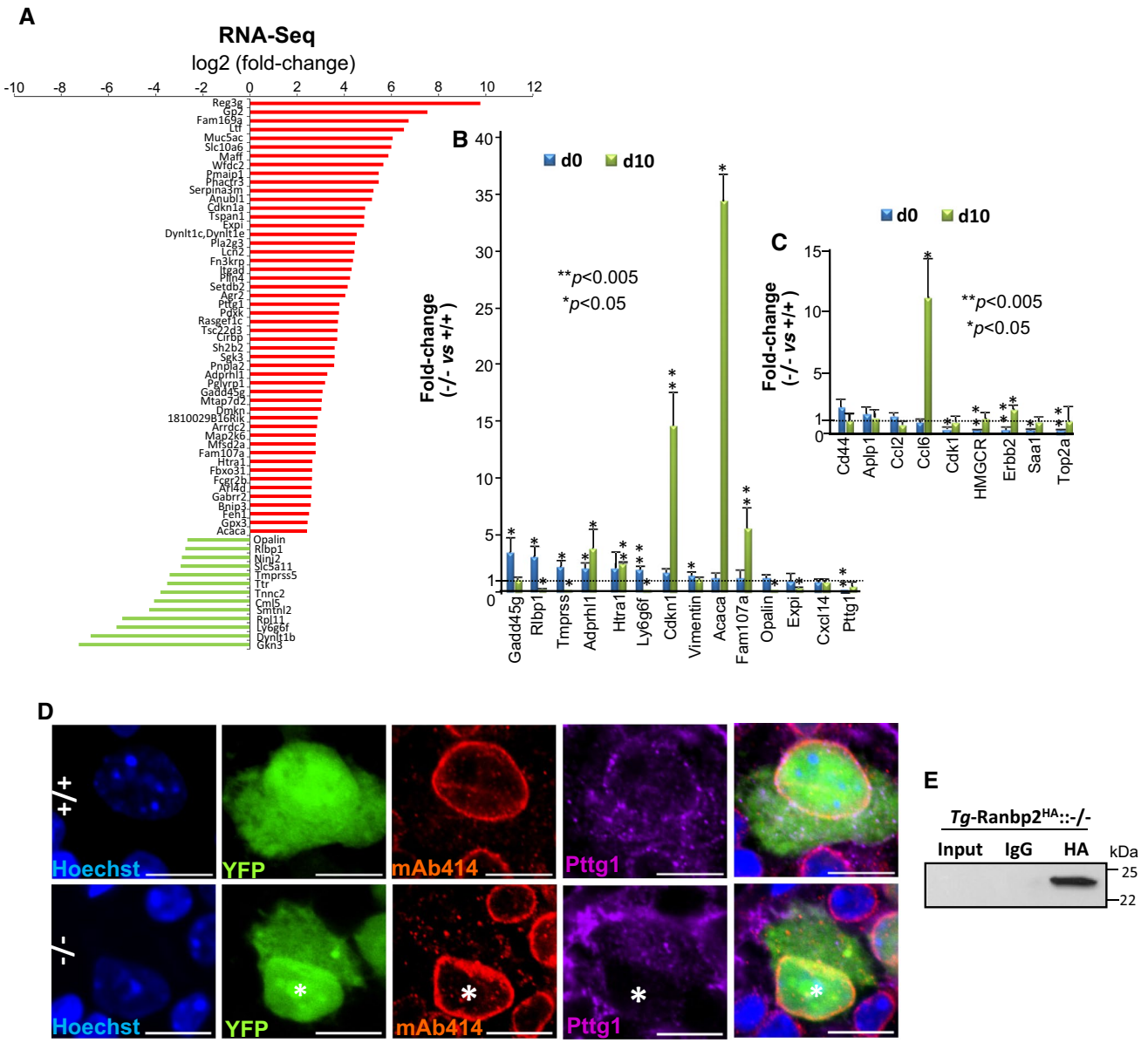


**Fig. 5** Differential transcriptome and gene expression analyses of optic nerve of retinal ganglion neurons (RGNs) upon loss of *Ranbp2*. **A** Differential RNA-Seq-based whole-transcriptome analysis of optic nerves between *SLICK-H::Ranbp2*$^{flox/flox}$ (−/−), *SLICK-H::Ranbp2*$^{+/+}$ (+/+) and *Tg*$^{RBD2/3*\text{-}HA}$*::SLICK-H::Ranbp2*$^{flox/flox}$ at day 10 post-tamoxifen administration. Fifty transcripts were up-regulated (red) and thirteen transcripts were down-regulated in −/− mice at d10. **B** Validation of ranked RNA-Seq dataset by RT-qPCR and temporal and directional changes of expression levels of mRNAs between −/− and +/+ mice. Thirteen transcripts were validated to be up-regulated and *Pttg1* was validated to be down-regulated by RT-qPCR in −/− mice at d0, d10 or both. *Acaca* (acetyl-CoA carboxylase alpha; also known as Acc1) and cdkn1 (cyclin-dependent kinase inhibitor 1) had the strongest up-regulation (~35 and 15-fold, respectively) at d10, whereas Pttg1 was down-regulated by ~25-fold at d0. Data are expressed as mean ± SD. Student's *t* test, *n* = 3–4 mice/genotype. **C** Temporal and directional changes of expression of mRNAs in the optic nerve between -/- and +/+ mice and whose levels are known to be changed in the sciatic nerve by loss of *Ranbp2*. Five genes (*Ccl6*, *Cdk1*, *HMGCR*, *erbb2*, *Saa1* and *Top2a*) were found also to be dysregulated in the optic nerve on d0, d10, or both. *Ccl6* had the strongest change of expression (~11-fold increase). Data are expressed as mean ± SD. Student's *t* test, *n* = 3–4 mice/genotype. **D** Confocal images of retinal flat mounts (ganglion neurons facing up) co-immunostained for Ranbp2 (Nup358)/Nup153/Nup62 (mAb414) and Pttg1. Pttg1 localizes at the nuclear rim with Ranbp2 (Nup358)/Nup153/Nup62 in YFP$^{+}$-RGNs of +/+ mice, while Pttg1 localization is lost at the nuclear rim of YFP$^{+}$-RGNs (nuclei labeled with *) of −/− mice. Scale bar 5 µm. **E** HA-tagged Ranbp2 (*Tg*-Ranbp2$^{HA}$) expressed in transgenic mice with a *null Ranbp2* background (−/−) co-immunoprecipitates Pttg1 from retinal extracts. Pttg1 is not detected in an overloaded aliquot of input extracts (first lane) owing to its very low abundance in retinal extracts. −/− *SLICK-H::Ranbp2*$^{flox/flox}$, +/+ *SLICK-H::Ranbp2*$^{+/+}$, *Tg-Ranbp2*$^{HA}$*:: −/− Tg-Ranbp2*$^{HA}$*::Ranbp2*$^{-/-}$, d0 and d10 days 0 and 10 post-tamoxifen administration, respectively

and temporal changes of the RNA-seq transcripts in optic nerves between genotypes at d0 and d10 by quantitative reverse transcription PCR (RT-qPCR) (Fig. 5B). Among these transcripts, RT-qPCR analysis validated 13 transcripts that were differentially modulated between genotypes on d0, d10 or both (Fig. 5B). We found that the transcripts with the highest up-regulation by d10 were acetyl-CoA carboxylase 1 (Acc1; ~ 35-fold, $p$ value < 0.05), cyclin-dependent kinase inhibitor 1A (Cdkn1a; ~ 15-fold, $p$ value < 0.05) and Family with sequence similarity 107/Down-regulated in renal cell carcinoma 1 (Fam107a/Drr1; ~ 6-fold, $p$ value < 0.05). Among the transcripts with the highest down-regulation were the mammalian-specific myelin and paranodal protein, opalin (~ 0.14-fold at d10, $p$ value < 0.05), the pituitary tumor-transforming gene I/securin (Pttg1; ~ 0.04-fold at d0, $p$ value < 0.05) and lymphocyte antigen 6 family member G6F (Ly6g6f; ~ 0.10-fold at d10, $p$ value < 0.05) (Fig. 5B). Notably, none of the transcripts differently regulated by Ranbp2 in the optic nerve overlapped with those that we previously reported by the same exact parameters in the sciatic nerve of the same mice [34]. To confirm further the cell-type specific effects of Ranbp2 between RGNs and motoneurons, we rescreened by RT-qPCR the optic nerve for transcriptional changes found to be modulated by Ranbp2 in the sciatic nerve [34]. We found only 6 transcripts with significant transcriptional changes between sciatic and optic nerves. However, and with the exception of chemokine (C–C motif) ligand 6 on d10 (Ccl6; ~ 11-fold, $p$ value < 0.05), the magnitude of the transcriptional changes were minor and below the cut-off used for differential analysis (< twofold) (Fig. 5C).

Given that the anti-apoptotic protein, Pttg1/securin, is a nuclear shuttling factor [67], we used the transcriptome findings to pursue the validation of this protein as a substrate of Ranbp2. We examined first its subcellular localization with the nucleoporins, Ranbp2/Nup358, Nup153 and Nup62, at the nuclear pore complexes (NPCs) of YFP$^+$-RGNs of wild type and *SLICK-H::Ranbp2*$^{flox/flox}$. As shown in Fig. 5D, the YFP$^+$-RGNs of wild-type mice showed prominent localization of Pttg1/securin with NPCs at the nuclear rim. In comparison, the nuclear rims of YFP$^+$-RGNs of *SLICK-H::Ranbp2*$^{flox/flox}$ mice lacked any immunostaining of Pttg1/securin. Then, to examine the association of Pttg1/securin with Ranbp2, we performed co-immunoprecipitation assays with a transgenic line expressing a wild-type *Ranbp2* transgene tagged with HA in a *null* background [33] (Fig. 5E). We found that Ranbp2 co-immunoprecipitated Pttg1/securin even though the abundance of Pttg1/securin was extremely low and could not be detected in immunoblots overloaded with aliquots of retinal extracts (Fig. 5E). This outcome likely reflects the low abundance of Pttg1/securin in RGNs and the very low representation of RGNs in the retinal neurome.

## Loss of Ranbp2 in YFP$^+$-RGNs causes the paracrine activation of microglia

As described, the differential expression analyses between genotypes uncovered that acetyl-CoA carboxylase 1 (Acc1) had the strongest up-regulation (~ 35-fold) in optic nerves of YFP$^+$-RGNs of *SLICK-H::Ranbp2*$^{flox/flox}$ mice. Acc1 is a critical fatty acid biosynthetic, rate-limiting and cytosolic isozyme, which mediates the conversion of acetyl-CoA to malonyl-CoA, a critical carbon donor for the synthesis of long-chain fatty acids [68, 69]. Acc1 is under tight post-translational and allosteric regulation and represents a critical metabolic switch in response to microenvironmental cues [69]. In particular, Acc1 was found recently to control T cell immunity [70, 71]. For example, suppression of Acc1 impairs the proliferation of CD8$^+$ T cells [70] and the formation of interleukin-17-secreting T cells of T-helper 17 ($T_H17$), while promoting the differentiation of anti-inflammatory and regulatory T cells ($T_{reg}$) [71]. In the central nervous system, $T_{reg}$ harbor alternative regenerative capacity by promoting remyelination and oligodendrocyte differentiation [72].

We examined the effects of loss of Ranbp2 in YFP$^+$-RGNs in neuroimmunity by analyzing the paracrine stimulation of resident macrophages of the CNS, the microglia. In this respect, we used retinal whole mounts immunostained with steady-state markers of microglia, such as CD11b and CD45, to examine the expression of these markers and morphological changes in microglia caused by loss of Ranbp2 in YFP$^+$-RGNs. The expression levels of CD11b and CD45 have been used to differentiate resting from activated parenchymal microglia [73]. Comparisons of retinae of wild type and *SLICK-H::Ranbp2*$^{flox/flox}$ mice by en face confocal microscopy showed that the retinal ganglion cell layer of *SLICK-H::Ranbp2*$^{flox/flox}$ mice had stronger CD11b$^+$ (Fig. 6A) and CD45$^+$-immunostaining (Fig. 6B) of ramified microglia than wild type mice (see also Supplementary Fig. 1).

The transformation of microglia from resting to active states is also known to be accompanied by changes in morphological phenotypes that is characterized by activated microglia losing their ramified or pseudopodial processes and gaining amoeboid appearances [73–75]. Hence, we used another marker for activated microglia, F4/80, to investigate morphological transformations in microglia caused by loss of Ranbp2 in YFP$^+$-RGNs. As shown in Fig. 7A, we observed that the RGN layer of wild type mice had intermingled F4/80$^+$-cell bodies of various sizes, whereas scanning of the RGN layer of *SLICK-H::Ranbp2*$^{flox/flox}$ mice indicated that there was a higher abundance of F4/80$^+$-cell bodies and that some of these cells had developed an amoeboid morphology. In light of the apparent non-uniform morphology of F4/80$^+$-microglia between wild type and

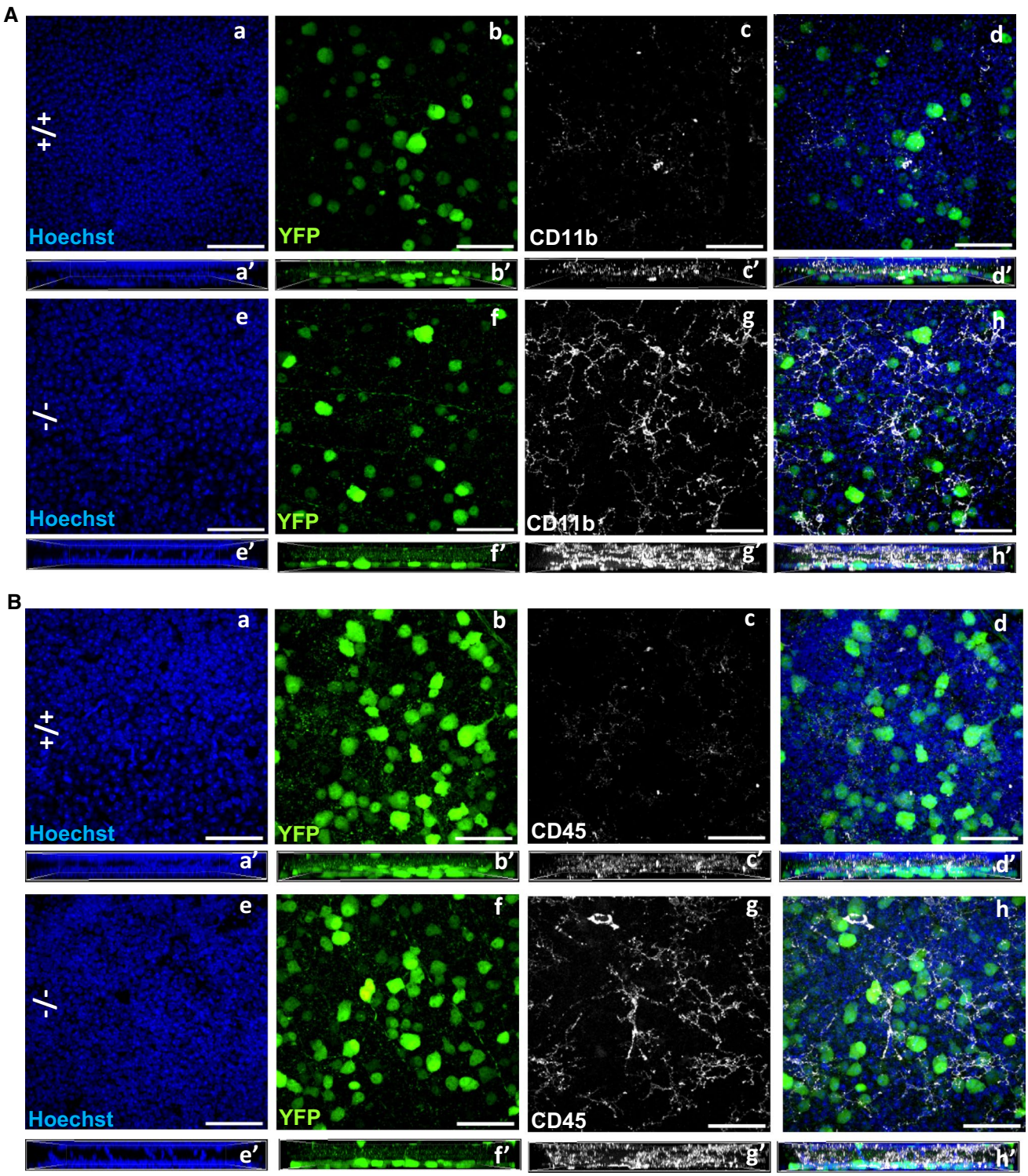


**Fig. 6** Activation of CD11b$^+$ and CD45$^+$-microglia in the ganglion cell layer of the retina by loss of *Ranbp2* in RGNs. Confocal images of retinal flat mounts (ganglion neurons facing up) of +/+ and −/− mice immunostained for CD11b (**A**) and CD45 (**B**) on d10. Compared to +/+ (**A**, **a**–**d**), there is prominent activation of CD11b$^+$-microglial cells, whose proliferative processes surround YFP$^+$-RGNs of −/− mice (**A**, **e**–**h**). Compared to +/+ (**B**, **a**–**d**), there is also prominent activation of CD45$^+$-microglial cells, whose proliferative processes surround YFP$^+$-RGNs of −/− mice (**B**, **e**–**h**). Figures **a′**–**h′** in **A** and **B** represent lateral views of *z*-stacks of **a**–**h** and collapsed from a 25 µm thick-stack of 13 images captured 2 µm apart. Scale bars 50 µm. *d10* day 10 post-tamoxifen administration, −/− *SLICK-H::Ranbp2$^{flox/flox}$*, +/+ *SLICK-H::Ranbp2$^{+/+}$*

*SLICK-H::Ranbp2*$^{flox/flox}$ mice, we carried out morphometric analysis of F4/80$^+$-microglia between genotypes. We found that *SLICK-H::Ranbp2*$^{flox/flox}$ had a ~ twofold increase of F4/80$^+$-microglia compared to wild type mice (Fig. 7B; $p < 0.04$). Then, we decomposed F4/80$^+$-microglia intermingled between YFP$^+$-RGNs based on their size. We found changes in the size of a subset of F4/80$^+$-microglia between genotypes. In comparison to wild-type mice, *SLICK-H::Ranbp2*$^{flox/flox}$ mice had significant ~ 2 ($p < 0.02$) and ~ 4-fold ($p < 0.01$) increases of amoeboid-like F4/80$^+$-microglia with sizes of ~ 50 and ~ 100 μm$^2$ and that these increases were accompanied by a significant ~ 3-fold ($p < 0.01$) decrease of F4/80$^+$-microglia with extended lamellipodial/pseudopodial-like processes and sizes of ~ 400 μm$^2$ (Fig. 7C).

### Loss of Ranbp2 causes the intracellular sequestration of Mmp-28 in YFP$^+$-RGNs of *SLICK-H::Ranbp2*$^{flox/flox}$

Our studies have uncovered that Ranbp2 controls the proteostasis and activities of Mmp11 and Mmp28 in a neuronal type-dependent manner and these effects culminate in non-cell autonomous responses [32, 34, 48]. For example, loss of Ranbp2 in Thy1$^+$-motoneurons promotes the down-regulation of Mmp28 in the sciatic nerve without affecting the secretion of Mmp28 from somata of Thy1$^+$-motoneurons [34]. Mmp28 is a regulator of macrophage activation and myelination [76–79]. In light of the foregoing findings, including that Mmp28 likely mediates neuronal-type-selective paracrine responses upon loss of Ranbp2, we examined the effects of loss of Ranbp2 in YFP$^+$-RGNs in the proteostasis and subcellular distribution of Mmp28. As shown in Fig. 8A, there was a significant decrease of the levels of a 90 kDa isoform (dimer) of Mmp28 in optic nerves of *SLICK-H::Ranbp2*$^{flox/flox}$ mice on d0 ($p < 0.05$) and d10 ($p < 0.005$), whereas this isoform of Mmp28 was transiently decreased in the retina on d0 only ($p < 0.05$). By contrast, the levels of a 48 kDa isoform (monomer) of Mmp28 was not significantly changed in optic nerves between genotypes and this Mmp28 isoform was not detected in the retina. Then, we examined the subcellular distribution of Mmp28 in YFP$^+$-RGNs between genotypes. Mmp28 was found prominently in the interstitial space between YFP$^+$-RGNs of wild-type mice, whereas there was widespread sequestration of Mmp28 in the intracellular compartment of YFP$^+$-RGNs of *SLICK-H::Ranbp2*$^{flox/flox}$ mice (Fig. 8B).

## Discussion

Mounting evidence support that dysregulation of nucleocytoplasmic trafficking is present in heterogeneous forms of sALS and fALS [1–10] and that the visual pathway, including RGNs, develop structural and functional impairments that may precede the development of ALS motor syndromes [6, 42–45]. Ranbp2 is a unique vertebrate nucleoporin, which controls rate-limiting steps of nucleocytoplasmic transport [10]. Ranbp2 is highly expressed in motoneurons and RGNs [10, 34, 35]. In the present study, a mouse model of ALS with rapid declines of motor performance that culminate in hind paralysis, respiratory distress and death, and without expression of Ranbp2 in Thy1$^+$-motoneurons and RGNs [34], was used to examine the roles of Ranbp2 in Thy1$^+$-RGNs. This disease mouse model represents a valuable tool to discern shared and unique molecular, cellular and pathobiological effects and pathognomonic signs of motoneuron disease, such as ALS, in RGNs and motoneurons [34].

The findings of this study support the following concepts. (1) Akin to many other cell types [10], RGNs and motoneurons share the dysregulation of nucleocytoplasmic transport by loss of *Ranbp*2. This disruption is manifested by the impairment of nucleocytoplasmic partition of Ran GTPase and nuclear import (e.g., importin-β) and export receptors (e.g., CRM1/exportin-1) and auxiliary substrates (e.g., HDAC4). (2) Ranbp2 is critical to RGN homeostasis; the somas of Thy1$^+$-RGNs develop hypertrophy and their myelinated axons undergo a decline of axonal caliber following deletion of *Ranbp2*. These effects are accompanied by a functional delay of visual cortical responses to light stimuli. (3) With the exception of Ccl6, the optic nerve does not co-opt transcriptome changes with the sciatic nerve after loss of *Ranbp2* in RGNs and motoneurons [34]. Loss of Ranbp2 in RGNs induces the pronounced and significant increase of the mRNA level of a critical immunomodulator, acetyl-CoA carboxylase 1 (Acc1), which is known to control de novo fatty acid synthesis and immunity in T cells [70, 71]. In naive mice lacking Ranbp2 in RGNs, the up-regulation of Acc1 was accompanied by activation of microglia. (4) RGNs and motoneurons share the dysregulation of the proteostasis of Mmp28, which is another modulator of immunity and possibly myelination [76–79], but this effect likely arises by distinct mechanisms between RGNs and spinal motoneurons.

Like in spinal motoneurons [34] and other cell types [10, 32], the nucleocytoplasmic partitioning of the driver of nucleocytoplasmic transport, Ran GTPase, and nuclear import (importin-β) and export receptors (e.g., CRM1/exportin-1), were impaired in RGNs lacking Ranbp2 of *SLICK-H::Ranbp2*$^{flox/flox}$. Comparable disruptions were also observed in auxiliary substrates of Ranbp2 (e.g., HDAC4 and NR2F2). These observations are consistent with the regulation of rate-limiting steps of disassembly of nuclear export ensembles by Ranbp2 [10, 18, 20, 23–25]. Unexpectedly, loss of Ranbp2 in RGNs caused transcriptome changes in optic nerves that were distinct from those previously reported for the sciatic nerve of motoneurons lacking

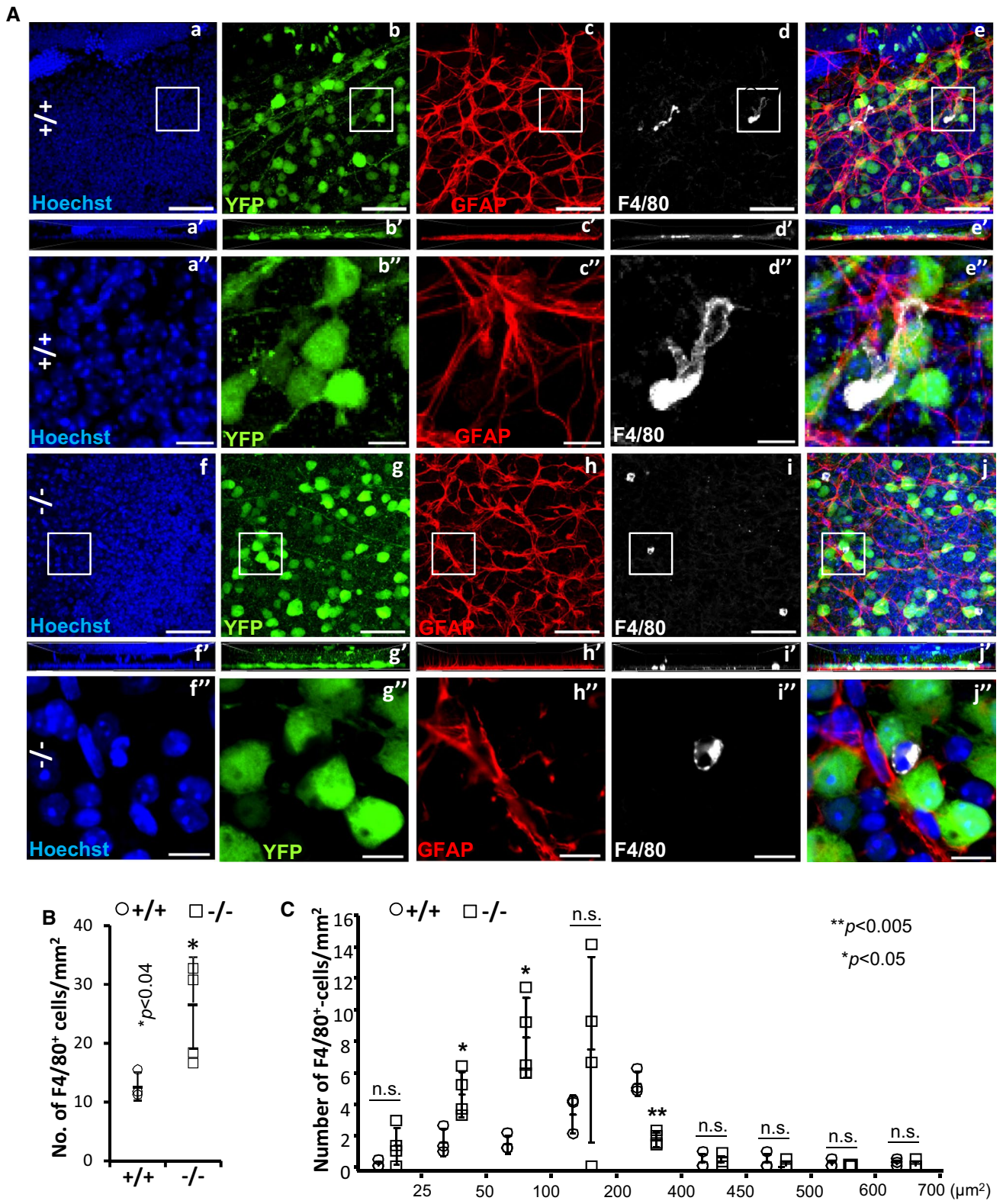


*Ranbp2* [34]. These findings support a combinatorial coding mechanism whereby Ranbp2 regulates the nucleocytoplasmic transport of neuronal-type selective substrates and whose nuclear export or import is dependent on exportin-1, importin-β or both. It is unlikely that the nuclear import pathway plays a determinant pathophysiological role in motoneurons and RGNs lacking Ranbp2, because genetic complementation studies support that mice with loss of

◂**Fig. 7** Activation of F4/80$^+$-microglial in the ganglion cell layer of the retina by loss of *Ranbp2*. **A** Confocal images of retinal flat mounts (ganglion neurons facing up) of +/+ and −/− mice immunostained for GFAP and F4/80 on d10. F4/80$^+$-microglia in the retinae of +/+ mice present extended pseudopodial-like processes (**a**–**e**), whereas −/− have a significant increase of the number of activated and smaller F4/80$^+$-microglia with an amoeboid morphology (**f**–**j**). Images **a″**–**j″** are magnified images of inset boxes in images **a**–**j**. There is no apparent astrogliosis between −/− and +/+ as reflected by the lack of overt changes in immunolabeling of GFAP$^+$-astrocytes between −/− (**h**–**h″**) and +/+ (**c**–**c″**). Images **a′**–**j′** are lateral views of *z*-stacks of **a**–**j** and collapsed from a 25 µm thick-stack of 13 images captured 2 µm apart. F4/80$^+$-microglia of −/− show a clear and typical amoeboid morphology of activation (inset box in **i** is magnified in **i″**), whereas resting F4/80$^+$-microglia of +/+ show prominent morphological extended processes like lamellipodia/pseudopodia (inset box in **d** is magnified in **d″**). **B** Quantitative analyses of F4/80$^+$-microglia showing that there is a significant increase of the number of F4/80$^+$-microglia in the ganglion cell layer of −/− compared to +/+ mice. Data are expressed as mean ± SD. Student's *t* test, $n=3$ (+/+) and $n=4$ (−/−) mice/genotype. **C** Quantitative analysis of the distribution of size (areas) of F4/80$^+$-microglia between genotypes show that the ganglion cell layer of −/− mice have a significant shift from a pool of F4/80$^+$-microglia with an average size of 400–450 µm$^2$ to a pool of F4/80$^+$-microglia with an average size of 25–100 µm$^2$. Data are expressed as mean ± SD. Student's *t* test, $n=3$ (+/+) and $n=4$ (−/−) mice/genotype. Scale bars 50 µm (**a**–**j**), 10 µm (**a″**–**j″**). *d10* day 10 post-tamoxifen administration, *n.s.* non-significant, −/− *SLICK-H::Ranbp2$^{flox/flox}$*, +/+ *SLICK-H::Ranbp2$^{+/+}$*

Ran-GTP and importin-β-binding to RBD2 and RBD3 of Ranbp2 (e.g.; *Tg-Ranbp2$^{RBD2/-HA}$::SLICK-H::Ranbp2$^{flox/flox}$*) rescue the motor behavior developed by mice with loss of *Ranbp2* in motoneurons [34]. This is in contrast to the severe degeneration of other cell types caused by similar loss of function of RBD2 and RBD3 of Ranbp2 (e.g., retinal pigment epithelium and developing cone photoreceptor neurons) [32].

A possible scenario is that impairment of a Ranbp2-mediated nuclear export pathway by uncoupling the docking of exportin-1 to the zinc-finger cluster domain of Ranbp2 in RGNs and motoneurons lacking *Ranbp2* precludes the bridging of nuclear export and axonal transport of selective ribonucleic protein cargoes (e.g., mRNPs) that are unique to RGNs and motoneurons [10, 20]. Motoneurons and RGNs are likely very vulnerable to impairments in the coupling of nuclear export with axonal transport because of the burden harbored by these neurons for the very long-distance transport of cargoes between somata and synapses in axons, such as of the sciatic nerve and whose linear length can reach a meter in size [10, 80]. This concept is supported by several findings. First, haploinsufficiency or missense mutations in the nucleoporin, *Gle1*, which mediates nuclear export of mRNAs, cause fetal motoneuron disease or ALS [81]. Second, the motor activities of the microtubule-based motor and kinesin-1 isoforms, KIF5B/KIF5C, which mediate the anterograde transport of selective cargoes, are regulated directly by Ranbp2 [82–85]. Third, Ranbp2 via its ZnF-cluster domain and docking of exportin-1 to ZnF (Fig. 4A) potentiates the nuclear export of selective mRNAs from the nucleus and their translations [20–22]. Finally, loss of Ranbp2 in motoneurons causes pronounced increases of the levels of selective mRNAs and decreases of their translation products. This outcome may result from the uncoupling of transport and translation of these mRNAs after loss of Ranbp2 at the nuclear pores and thereby promoting the hypertrophy of somata of motoneurons and axonopathy of the sciatic nerve [34]. These effects may also be shared by RGNs with pronounced dysregulation of limited mRNAs, such as *Acc1*, in the optic nerve and that may contribute to hypertrophy of somata of RGNs and axonopathy of the optic nerve.

Contemporary and recent studies indicate RGN involvement in ALS [6, 42–45]. Specifically, these studies have shown that ALS is associated with structural changes by the thinning of the nerve fiber layer (e.g., unmyelinated axons of RGNs before they exit the optic cup), histopathological changes in inner retinal neurons, and functional deficits in sensory processing of the visual pathway to the brain measured by pattern reversal or luminance-evoked VEPs [6, 42–45]. Even though prior studies found that Ranbp2 plays critical physiological roles in the function and survival of photoreceptor neurons [48, 55], we have found that mice with decreased levels of hnRNPA2B1 in the inner retina caused by selective loss of peptidyl *cis–trans* prolyl isomerase activity of Ranbp2 across all retinal neurons develop shorter latency of dark-adapted VEPs without changes in the electroretinograms generated from neurons of the outer retina (e.g., photoreceptor neurons) [33]. In this study, we found that loss of Ranbp2 in RGNs was accompanied structurally by a decline of axonal diameter without loss of RGNs and functionally by a delay of the implicit times (latency) of VEPs before changes of motor behavior ensue [34], but without changes of VEP amplitudes. These results corroborate that the lack of untoward effects in VEP amplitudes of mice without Ranbp2 in RGNs reflect the generation of unperturbed and collective input responses to the visual cortex by a normal number of RGNs [60–62]. In contrast, the VEP latency of mice without Ranbp2 in RGNs support a delay in optic nerve conduction and thus transmission of the action potentials by the axons of the optic nerve to the visual cortex [42, 60–62]. Our results suggest that axonopathy and changes in *g*-ratios of the optic and sciatic nerves contribute to a decrease of nerve conduction [34]. Parenthetically, we have not found overt changes in the periodicity of nodes of Ranvier (e.g., $Na^+$-channel) in nerves of mice lacking Ranbp2 in motoneurons and RGNs. Further, the myelin and paranodal protein, opalin, whose transcriptional level is strongly reduced in the optic nerve of mice lacking Ranbp2 in RGNs, may also not contribute to the VEP latency, because mice lacking opalin expression do not present abnormalities in myelination and motor behavior [86].

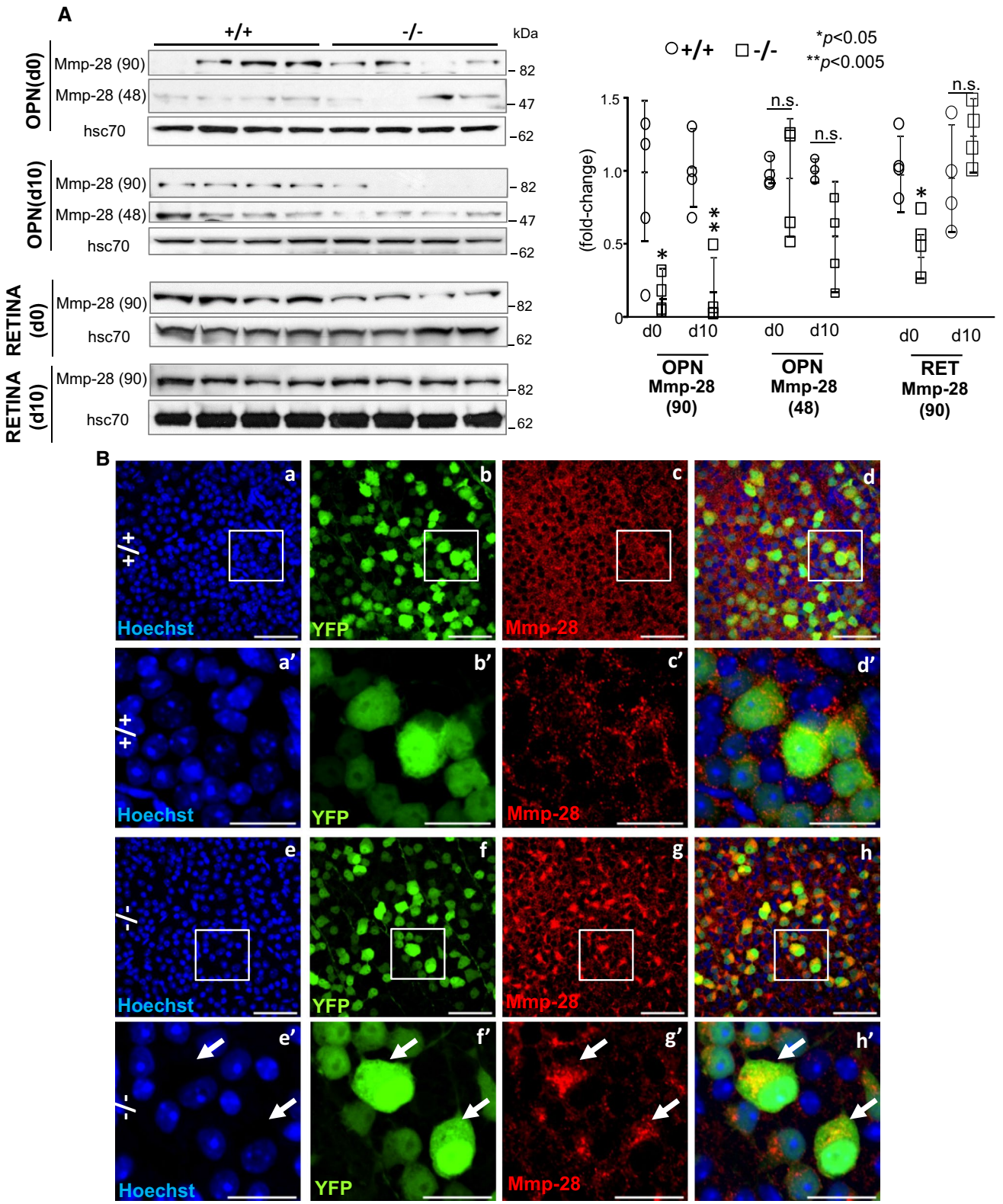


Although the exact molecular basis for the decline in nerve conduction by loss of *Ranbp2* will need further investigation, loss of *Ranbp2* in RGNs may also shed light to delays in VEP timing shared by other optic nerve diseases, such as glaucoma, which is also linked to ALS [87, 88], demyelinating diseases with optic nerve involvement and optic neuropathies [89–91].

◂**Fig. 8** Suppression of proteostasis and biogenesis of Mmp-28 in the optic nerve and retinal ganglion neurons (RGNs) by loss of *Ranbp2*. **A** Immunoblots (left) and quantitative analysis (right) of expression of the 90 (dimer) and 48 kDa (monomer) isoforms of Mmp-28 in the optic nerve (OPN) and retina (RET) on d0 and d10. In the optic nerve, −/− mice present a decline of the 90 kDa of Mmp-28 [Mmp-28(90)] on d0 and d10, whereas there are no changes in the levels of the 48 kDa of Mmp-28 [Mmp-28(48)] on d0 and d10. In the retina, there is no expression of the Mmp-28(48) isoform and −/− mice have decreased levels of Mmp-28(90) on d0 only. Hsc70 is a loading control. Data are expressed as mean ± SD. Student's *t* test, $n = 4$ mice/genotype. **B** Confocal images of retinal flat mounts (ganglion neurons facing up) of +/+ (**a**–**d**, **a′**–**d′**) and −/− mice (**e**–**h**, **e′**–**h′**) immunostained for Mmp-28 at d10. Mmp-28 is localized outside somata of $YFP^+$-RGNs (extracellular space) of +/+ mice, whereas there is prominent and widespread intracellular sequestration of Mmp-28 in somata of $YFP^+$-RGNs of −/− mice (arrows). **a′**–**h′** are magnified images of inset regions of **a**–**h**. Scale bars 50 (**a**–**h**) and 20 µm (**a′**–**h′**). −/− *SLICK-H::Ranbp2*$^{flox/flox}$, +/+ *SLICK-H::Ranbp2*$^{+/+}$, *hsc70* heat shock protein 70, *d0 and d10* days 0 and 10 post-tamoxifen administration, respectively; *n.s.* non-significant, *OPN* optic nerve, *RET* retina

Recent studies have used transcriptome approaches to gain insights into the pathogenesis of ALS and the vulnerability of motoneurons to ALS [92]. In contrast to other ALS-causing RNA-binding proteins in which mutations purportedly promote broad transcriptome changes [93–95], knockdown of hnRNPA2B1 in the spinal cord led to the misregulation of a small number of transcripts (~ 20–30) [96]. Notably, little transcriptional overlap existed between the spinal cord and human iPSC-derived motor neurons [96]. Cultured spinal motoneurons expressing mutations in $SOD1^{G93A}$ and $TDP43^{A315T}$ showed few alterations in transcriptional expression and an overlap of only 20 transcripts that encoded proteins mainly with predicted extracellular localization [97]. Lumbar spinal motor and oculomotor neurons, which control eye movement and are spared in ALS, showed differences in broad transcriptional profiles of over 1700 genes and some of these presumably indicate a reduced vulnerability of oculomotor neurons to excitotoxicity by enhanced GABAergic transmission [98]. Finally, the transcriptome of microglia purified from spinal cord of ALS mice with $SOD1^{G93A}$ compared to wild-type mice showed that ~ 2000 transcripts are differential regulated by at least twofold at late stages of the disease [92]. Collectively, these studies support the notion that distinct genetic insults in ALS promote heterogeneous transcriptional responses; however, the pathobiological relevance and the extent to which experimental and disease contexts contribute to apparent divergences in transcriptional abnormalities remain unclear. In contrast, our study explored the effects of selective Ranbp2-mediated disruption of nucleocytoplasmic transport, which is shared by heterogeneous forms of sALS and fALS [1–10], in the transcriptome of the optic nerve. Further, we compared the transcriptome changes of the optic nerve with those previously reported for the sciatic nerve of the same mice with and without *Ranbp2* in RGNs and motoneurons [34].

Notably, our analysis showed that apart from *Ccl6*, there was no overlap between the transcriptomes of optic and sciatic nerves subjected to concurrent loss of *Ranbp2* in RGNs and motoneurons. The distinct ontologies between oligodendrocytes (e.g., neural tube) and Schwann cells (e.g., neural crest) that ensheath with myelin the axons of optic and sciatic nerves, respectively, may contribute to the absence of overlap in transcriptome changes [99]. In this respect, several transcripts, such as opalin (Tmem10) and Fam107a/Drr1, encode known glial markers of the CNS [100, 101], while others, such as Ly6g6f, are up-regulated in frontotemporal lobar degeneration (FTLD) and linked to atrophy of the superior frontal gyrus, neuroinflammation and immunity [102, 103]. Importantly, we found that the lipogenic enzyme, Acc1, was the target with the highest up-regulation in the optic nerve (~ 35-fold, $p$ value < 0.05). Acc1 up-regulation is at the crux of a metabolic shift in the de novo fatty acid synthesis pathway by converting acetyl-CoA to malonyl-CoA, which is the carbon donor for the synthesis of long-chain fatty acids [68, 69]. The stimulation of this pathway is critical to release the dependence of tumor cell growth and survival from exogenous lipids [104]. In contrast, Acc1 inhibition suppresses $CD8^+$ T-cell expansion [70] and the genesis of $T_H17$ cells with pathogenic roles in inflammatory and autoimmune diseases, but favors the differentiation of anti-inflammatory $T_{reg}$ cells, whose differentiation depends on exogenous fatty acids [71].

Our study found that in the CNS (retina) the pronounced up-regulation of *Acc1* mRNA was associated to the activation of microglia as manifested by the activation of ramified $CD11b^+$ and $CD45^+$-microglia, increase of $F4/80^+$-microglia and development of amoeboid $F4/80^+$-microglia intermingled between RGNs lacking Ranbp2 of naive mice. It is possible that an increased shift in dynamics between pseudopodial/lamellipodial and amoeboid $F4/80^+$-microglia contributes to the increase of amoeboid $F4/80^+$-microglia [75]. Current studies indicate that native insults (e.g., genetic mutations) to the CNS, such as retina, promote the activation of resident microglia without involvement of perivascular and systemic macrophages [75, 105, 106]. In contrast, non-native insults (e.g., irradiation, excitotoxicity, etc.) promote the infiltration of perivascular and systemic macrophages likely by disturbances or disruption of the blood-retinal/brain barrier [107, 108]. Hence, these data suggest that the activation of microglia by the native insult comprised of loss of *Ranbp2* in RGNs arises from resident microglia rather than from the infiltration of perivascular/systemic macrophages. Further, the infiltration of perivascular/systemic macrophages to the retina triggered by non-native insults is delayed well beyond the time that it takes for microglial activation to occur in the retina of mice lacking

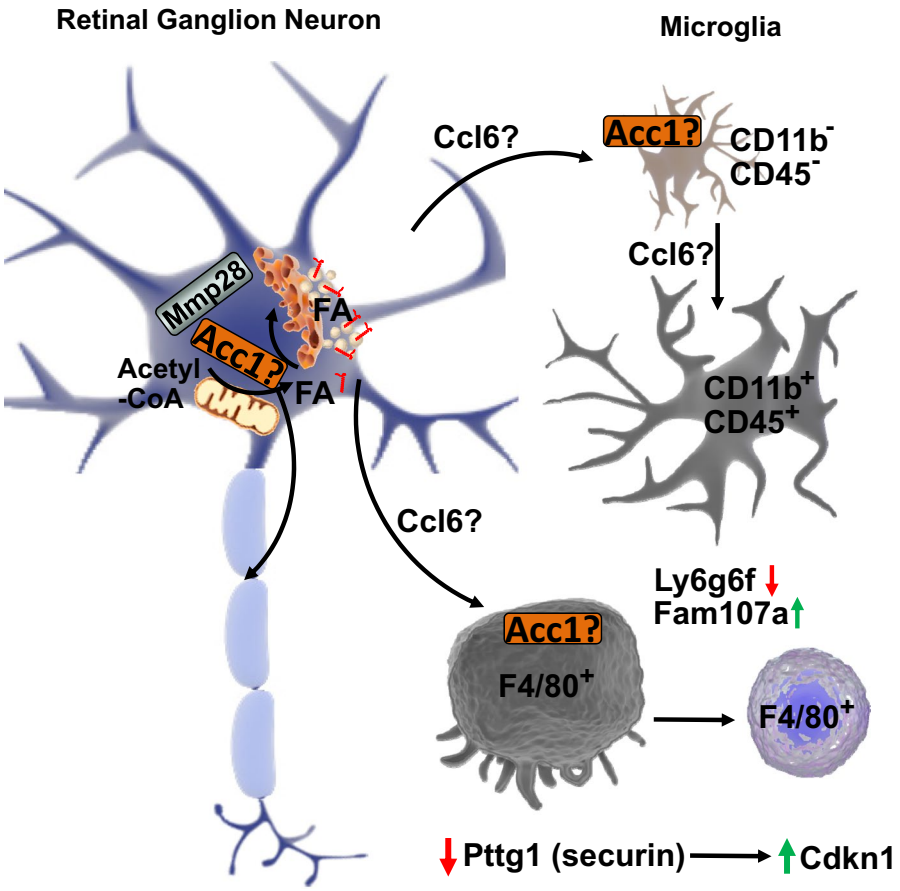


**Fig. 9** Mechanistic model of microglial activation by loss of Ranbp2 in Thy1-retinal ganglion neurons (RGNs). Loss of *Ranbp2* in RGNs triggers the up-regulation of *Acc1* and the stimulation of free fatty acids and/or Ccl6 in RGNs, microglia or both. There is also intracellular sequestration of Mmp28 in RGNs that relieves the suppression of Ccl6 production and stimulates neuron-glia signaling and the multiphasic activation of microglia with $CD11b^+$ and $CD45^+$-ramified and $F4/80^+$-amoeboid morphologies. These effects are accompanied by changes in expression of cell-cycle and surface antigen/cell migration regulators, such as the down-regulation of Pttg1 and Ly6g6f and the up-regulation of Cdkn1 and Fam107a in RGNs and/or microglia (see text for details)

*Ranbp2* in RGNs (< 10 days) [107, 108]. Hence, the *Ranbp2* mouse model herein described will provide another venue to investigate the origins and spatiotemporal mechanisms of microglial activation by native insults. Regardless, our results suggest the activation of a non-cell autonomous (paracrine) signaling mechanism between RGNs and quiescent microglia resident in the retina that is mediated by the Acc1 production of free-fatty acids in RGNs. An analogous chemokine-mediated paracrine signaling between axons of spinal motoneurons and surrounding Schwann cells appears also to be triggered by loss of *Ranbp2* in motoneurons [34].

In contrast to our findings in the sciatic nerve [34] and other neurons [55] however, we did not find changes in the levels of free fatty acids (octanoate and longer fatty acids) in the optic nerve [34]. The reason for this outcome needs further investigation, but it is possible that distinct species of free fatty acids are produced by Acc1 in RGNs or oligodendrocytes, or between RGNs and motoneurons, and that these cell-type and/or insult-selective and elicited species mediate distinct non-cell autonomous responses. In this regard, metabolomics studies found that brains of haploinsufficient *Ranbp2* mice when challenged with the parkinsonian neurotoxin, MPTP, presented a decline of the medium-chain free fatty acids, pelargonate (9:0) and caprate (10:0), and of the long-chain free fatty acid, arachidate (20:0), and that these effects were associated with robust astrogliosis in the retina [53]. Alternatively, emerging studies indicate that suppression of Acc1 also plays a fatty acid synthesis-independent role by promoting acetyl-CoA-dependent acetylation of proteins that trigger selective cellular responses. It is noteworthy that both motoneurons and RGNs share the nucleocytoplasmic deregulation of HDAC4, which is a substrate of Ranbp2 [33, 34, 65]. Hence, an increase of Acc1 levels combined with dysregulation of HDAC4 may result in the dysregulation of acetylation of selective substrates that ultimate contribute to the activation of microglia. This study will provide the foundation to elucidate between these mechanistic scenarios that are not mutually exclusive necessarily.

Recent studies support the notion that selective metalloproteinases act directly as strong modifiers of disease progression in ALS and cytokine-mediated pathology [109, 110]. Our prior studies have shown that Ranbp2 controls the proteostasis of selective metalloproteinases (e.g., Mmp11 and Mmp28) in a neuronal-type dependent manner and that these Mmps are prime candidates to exert non-cell autonomous effects in neighboring cells/tissues [32, 34, 48]. In motoneurons, Ranbp2 regulates Mmp28 proteostasis in the sciatic nerve but not in somata of motoneurons [34]. This

study in accord to other studies found that Mmp28 is constitutively secreted to the interstitial space of the ganglion neuronal network of the retina. Mmp28 is a known regulator of peripheral immune responses involving M1 and M2 type macrophages by mechanisms that remain elusive [76, 77, 111]. However, the physiological role(s) of Mmp28 in the CNS is unknown. Our studies suggest that the regulation of Mmp28 expression by *Ranbp2* may control the proteostasis of substrates that act as mediators in RGN-microglial signaling. In this regard, the up-regulation of Acc1 by loss of *Ranbp2* in RGNs may contribute to the intracellular sequestration of Mmp28 by affecting the biogenesis of the endoplasmic reticulum and Golgi apparatus and membrane phospholipids [71, 112]. However, ultrastructural analysis of somata of RGNs did not find overt ER/Golgi pathologies. Alternatively, the dysregulation of Mmp28 proteostasis by loss of *Ranbp2* in RGNs may alter the balance between anti-inflammatory or pro-inflammatory cytokines in the interstitial space and thereby promoting microglial activation. To this effect, Ccl6 is a chemokine whose production is strongly stimulated in inflammatory disorders [113, 114] and its up-regulation is shared by motoneurons and RGNs upon loss of *Ranbp2* [34]. Ccl6 acts as a macrophage chemoattractant [114] and Ccl6 is also expressed by microglia [115]. Since challenged macrophages lacking Mmp28 present enhanced chemotaxis and chemokine production [76, 77], suppression of Mmp28 biogenesis in RGNs may stimulate Ccl6 and activate RGN-to-microglial signaling (microglial activation) and/or a signaling loop between microglia. The studies herein reported will provide a framework to investigate the independent contributions of Acc1 and Mmp28 toward the activation of microglia, and potential subtypes thereof, in the CNS by loss of *Ranbp2* in RGNs.

In summary, mechanistically our results support a model in which loss of Ranbp2 in RGNs promotes immune responses in the CNS that apart from Ccl6 and Mmp28 are distinct from the peripheral responses caused by loss of Ranbp2 in spinal motoneurons [34]. Our model indicates that Ranbp2 is a major regulator of *Acc1* and Mmp28 expressions and that Acc1 and Mmp28 may play a central role in neuroimmunity by controlling non-autonomous (paracrine) cell signaling between RGNs and microglia upon loss of Ranbp2 in RGNs (Fig. 9). According to this model, up-regulation of *Acc1* by loss of Ranbp2 inhibits the biogenesis (e.g., secretion) of Mmp28 and stimulates the release of selective chemokines (e.g., Ccl6) and/or fatty acids that promote neuronal-glial signaling and microglial priming and activation. These effects are accompanied by the biphasic regulation of the cell cycle protein, Pttg1/securin, and its potential transcriptional target, Cdnk1 (p21) [67], and of stress-signaling, cell migration and cell surface membrane markers, such as, Ly6g6f and Fam107a [101, 103, 116–118]. Hence, these targets are strong candidates to modulate the proliferation and migration of microglia. Although microglial dysfunction is linked to ALS [119], emerging and contradictory data also suggest that there is a lack of convergence in neuroinflammation between fALS and sALS [120]. Our data indicate that the disruption of nucleocytoplasmic transport shared by fALS and sALS, and between retinal ganglion and motor neurons, promotes unique endophenotypes in RGNs and microglia and that the visual pathway may offer pathognomonic signs of ALS and other motoneuron diseases. These molecular and cellular mechanisms deserve heightened attention because nucleocytoplasmic transport is also disrupted in other neurodegenerative diseases [11–14].

**Acknowledgements** We thank Guoping Feng (MIT, Cambridge, MA) for SLICK-H mice, Ian Macara (Vanderbilt University, Nashville, TN) for the antibody against Ran-GTP, Sandra Stinnett for help with statistical analyses of RGN morphometry (Duke University, Durham, NC), Ying Hao for help with the processing of the specimens for transmission electron microscopy (Duke University, Durham, NC).

**Author contributions** KC and PAF conceived and supervised the study; KC, NSP and PAF designed experiments; KC, MY and DY performed experiments; PAF provided new tools and reagents; KC, DY, NPS and PAF analyzed data; KC and PAF wrote the manuscript.

**Funding** The study was funded by National Institutes of Health Grants GM083165, GM083165-03S1 and EY019492 to P.A.F. This work was also supported by a Core Grant (P30 EY025585) to Cleveland Clinic Lerner College of Medicine of Case Western Reserve University and a Research Career Scientist Award to N.S.P. from the U.S. Department of Veterans Affairs.

## Compliance with ethical standards

**Conflict of interest** The author(s) declared no potential conflicts of interest with respect to the research, authorship, and/or publication of this article. All authors consent for the publication of this study.

**Availability of data and materials** The datasets supporting the conclusions of this article are available in the Sequence Reads Archives (SRA; https://www.ncbi.nlm.nih.gov/sra) of the National Center for Biotechnology Information (NCBI) with the accession number: SRP139153. Datasets of a total of ~17.4 billion bases of unprocessed RNA sequencing were deposited as FASTq files at the SRA. The project overview was deposited with the Bioproject accession number: PRJNA449172. The optic nerves of *SLICK-H::Ranbp2*$^{+/+}$, *SLICK-H::Ranbp2*$^{flox/flox}$ and *Tg-RBD*$^{2/3*-HA}$*::SLICK-H::Ranbp2*$^{flox/flox}$ have the respective biosamples accession numbers: SAMN08891694, SAMN08891693 and SAMN08891695. Other datasets and materials used and/or analyzed during the current study are available from the corresponding author on reasonable request.

## References

1. Zhang J, Ito H, Wate R, Ohnishi S, Nakano S, Kusaka H (2006) Altered distributions of nucleocytoplasmic transport-related proteins in the spinal cord of a mouse model of amyotrophic

lateral sclerosis. Acta Neuropathol 112(6):673–680. https://doi.org/10.1007/s00401-006-0130-4
2. Kinoshita Y, Ito H, Hirano A, Fujita K, Wate R, Nakamura M, Kaneko S, Nakano S, Kusaka H (2009) Nuclear contour irregularity and abnormal transporter protein distribution in anterior horn cells in amyotrophic lateral sclerosis. J Neuropathol Exp Neurol 68(11):1184–1192. https://doi.org/10.1097/NEN.0b013e3181bc3bec
3. Dormann D, Rodde R, Edbauer D, Bentmann E, Fischer I, Hruscha A, Than ME, Mackenzie IR, Capell A, Schmid B, Neumann M, Haass C (2010) ALS-associated fused in sarcoma (FUS) mutations disrupt Transportin-mediated nuclear import. EMBO J 29(16):2841–2857. https://doi.org/10.1038/emboj.2010.143
4. Xiao S, MacNair L, McGoldrick P, McKeever PM, McLean JR, Zhang M, Keith J, Zinman L, Rogaeva E, Robertson J (2015) Isoform-specific antibodies reveal distinct subcellular localizations of C9orf72 in amyotrophic lateral sclerosis. Ann Neurol 78(4):568–583. https://doi.org/10.1002/ana.24469
5. Nagara Y, Tateishi T, Yamasaki R, Hayashi S, Kawamura M, Kikuchi H, Iinuma KM, Tanaka M, Iwaki T, Matsushita T, Ohyagi Y, Kira J (2013) Impaired cytoplasmic-nuclear transport of hypoxia-inducible factor-1alpha in amyotrophic lateral sclerosis. Brain Pathol 23(5):534–546. https://doi.org/10.1111/bpa.12040
6. Ward ME, Taubes A, Chen R, Miller BL, Sephton CF, Gelfand JM, Minami S, Boscardin J, Martens LH, Seeley WW, Yu G, Herz J, Filiano AJ, Arrant AE, Roberson ED, Kraft TW, Farese RV Jr, Green A, Gan L (2014) Early retinal neurodegeneration and impaired Ran-mediated nuclear import of TDP-43 in progranulin-deficient FTLD. J Exp Med 211(10):1937–1945. https://doi.org/10.1084/jem.20140214
7. Freibaum BD, Lu Y, Lopez-Gonzalez R, Kim NC, Almeida S, Lee KH, Badders N, Valentine M, Miller BL, Wong PC, Petrucelli L, Kim HJ, Gao FB, Taylor JP (2015) GGGGCC repeat expansion in C9orf72 compromises nucleocytoplasmic transport. Nature 525(7567):129–133. https://doi.org/10.1038/nature14974
8. Zhang K, Donnelly CJ, Haeusler AR, Grima JC, Machamer JB, Steinwald P, Daley EL, Miller SJ, Cunningham KM, Vidensky S, Gupta S, Thomas MA, Hong I, Chiu SL, Huganir RL, Ostrow LW, Matunis MJ, Wang J, Sattler R, Lloyd TE, Rothstein JD (2015) The C9orf72 repeat expansion disrupts nucleocytoplasmic transport. Nature 525(7567):56–61. https://doi.org/10.1038/nature14973
9. Shang J, Yamashita T, Nakano Y, Morihara R, Li X, Feng T, Liu X, Huang Y, Fukui Y, Hishikawa N, Ohta Y, Abe K (2017) Aberrant distributions of nuclear pore complex proteins in ALS mice and ALS patients. Neuroscience 350:158–168. https://doi.org/10.1016/j.neuroscience.2017.03.024
10. Ferreira PA (2019) The coming-of-age of nucleocytoplasmic transport in motor neuron disease and neurodegeneration. Cell Mol Life Sci. https://doi.org/10.1007/s00018-019-03029-0 **(in press)**
11. Woerner AC, Frottin F, Hornburg D, Feng LR, Meissner F, Patra M, Tatzelt J, Mann M, Winklhofer KF, Hartl FU, Hipp MS (2016) Cytoplasmic protein aggregates interfere with nucleocytoplasmic transport of protein and RNA. Science 351(6269):173–176. https://doi.org/10.1126/science.aad2033
12. Grima JC, Daigle JG, Arbez N, Cunningham KC, Zhang K, Ochaba J, Geater C, Morozko E, Stocksdale J, Glatzer JC, Pham JT, Ahmed I, Peng Q, Wadhwa H, Pletnikova O, Troncoso JC, Duan W, Snyder SH, Ranum LPW, Thompson LM, Lloyd TE, Ross CA, Rothstein JD (2017) Mutant huntingtin disrupts the nuclear pore complex. Neuron 94(1):93–107 e106. https://doi.org/10.1016/j.neuron.2017.03.023
13. Gasset-Rosa F, Chillon-Marinas C, Goginashvili A, Atwal RS, Artates JW, Tabet R, Wheeler VC, Bang AG, Cleveland DW, Lagier-Tourenne C (2017) Polyglutamine-expanded huntingtin exacerbates age-related disruption of nuclear integrity and nucleocytoplasmic transport. Neuron 94(1):48–57 e44. https://doi.org/10.1016/j.neuron.2017.03.027
14. Eftekharzadeh B, Daigle JG, Kapinos LE, Coyne A, Schiantarelli J, Carlomagno Y, Cook C, Miller SJ, Dujardin S, Amaral AS, Grima JC, Bennett RE, Tepper K, DeTure M, Vanderburgh CR, Corjuc BT, DeVos SL, Gonzalez JA, Chew J, Vidensky S, Gage FH, Mertens J, Troncoso J, Mandelkow E, Salvatella X, Lim RYH, Petrucelli L, Wegmann S, Rothstein JD, Hyman BT (2018) Tau protein disrupts nucleocytoplasmic transport in Alzheimer's disease. Neuron 99(5):925–940 e927. https://doi.org/10.1016/j.neuron.2018.07.039
15. Cho KI, Orry A, Park SE, Ferreira PA (2015) Targeting the cyclophilin domain of Ran-binding protein 2 (Ranbp2) with novel small molecules to control the proteostasis of STAT3, hnRNPA2B1 and M-Opsin. ACS Chem Neurosci 6(8):1476–1485. https://doi.org/10.1021/acschemneuro.5b00134
16. Jovicic A, Mertens J, Boeynaems S, Bogaert E, Chai N, Yamada SB, Paul JW 3rd, Sun S, Herdy JR, Bieri G, Kramer NJ, Gage FH, Van Den Bosch L, Robberecht W, Gitler AD (2015) Modifiers of C9orf72 dipeptide repeat toxicity connect nucleocytoplasmic transport defects to FTD/ALS. Nat Neurosci 18(9):1226–1229. https://doi.org/10.1038/nn.4085
17. Boeynaems S, Bogaert E, Michiels E, Gijselinck I, Sieben A, Jovicic A, De Baets G, Scheveneels W, Steyaert J, Cuijt I, Verstrepen KJ, Callaerts P, Rousseau F, Schymkowitz J, Cruts M, Van Broeckhoven C, Van Damme P, Gitler AD, Robberecht W, Van Den Bosch L (2016) *Drosophila* screen connects nuclear transport genes to DPR pathology in c9ALS/FTD. Sci Rep 6:20877. https://doi.org/10.1038/srep20877
18. Delphin C, Guan T, Melchior F, Gerace L (1997) RanGTP targets p97 to RanBP2, a filamentous protein localized at the cytoplasmic periphery of the nuclear pore complex. Mol Biol Cell 8(12):2379–2390
19. Wu J, Matunis MJ, Kraemer D, Blobel G, Coutavas E (1995) Nup358, a cytoplasmically exposed nucleoporin with peptide repeats, Ran-GTP binding sites, zinc fingers, a cyclophilin A homologous domain, and a leucine-rich region. J Biol Chem 270(23):14209–14213
20. Singh BB, Patel HH, Roepman R, Schick D, Ferreira PA (1999) The zinc finger cluster domain of RanBP2 is a specific docking site for the nuclear export factor, exportin-1. J Biol Chem 274(52):37370–37378
21. Culjkovic-Kraljacic B, Baguet A, Volpon L, Amri A, Borden KL (2012) The oncogene eIF4E reprograms the nuclear pore complex to promote mRNA export and oncogenic transformation. Cell Rep 2(2):207–215. https://doi.org/10.1016/j.celrep.2012.07.007
22. Mahadevan K, Zhang H, Akef A, Cui XA, Gueroussov S, Cenik C, Roth FP, Palazzo AF (2013) RanBP2/Nup358 potentiates the translation of a subset of mRNAs encoding secretory proteins. PLoS Biol 11(4):e1001545. https://doi.org/10.1371/journal.pbio.1001545
23. Vetter IR, Nowak C, Nishimoto T, Kuhlmann J, Wittinghofer A (1999) Structure of a Ran-binding domain complexed with Ran bound to a GTP analogue: implications for nuclear transport. Nature 398(6722):39–46
24. Villa Braslavsky CI, Nowak C, Gorlich D, Wittinghofer A, Kuhlmann J (2000) Different structural and kinetic requirements for the interaction of Ran with the Ran-binding domains from RanBP2 and importin-beta. Biochemistry (Mosc) 39(38):11629–11639
25. Ritterhoff T, Das H, Hofhaus G, Schroder RR, Flotho A, Melchior F (2016) The RanBP2/RanGAP1*SUMO1/Ubc9 SUMO E3 ligase is a disassembly machine for Crm1-dependent

nuclear export complexes. Nat Commun 7:11482. https://doi.org/10.1038/ncomms11482
26. Mahajan R, Gerace L, Melchior F (1998) Molecular characterization of the SUMO-1 modification of RanGAP1 and its role in nuclear envelope association. J Cell Biol 140(2):259–270
27. Saitoh H, Pu R, Cavenagh M, Dasso M (1997) RanBP2 associates with Ubc9p and a modified form of RanGAP1. Proc Natl Acad Sci USA 94(8):3736–3741
28. Matunis MJ, Coutavas E, Blobel G (1996) A novel ubiquitin-like modification modulates the partitioning of the Ran-GTPase-activating protein RanGAP1 between the cytosol and the nuclear pore complex. J Cell Biol 135(6 Pt 1):1457–1470
29. Walther TC, Pickersgill HS, Cordes VC, Goldberg MW, Allen TD, Mattaj IW, Fornerod M (2002) The cytoplasmic filaments of the nuclear pore complex are dispensable for selective nuclear protein import. J Cell Biol 158(1):63–77
30. Hamada M, Haeger A, Jeganathan KB, van Ree JH, Malureanu L, Walde S, Joseph J, Kehlenbach RH, van Deursen JM (2011) Ran-dependent docking of importin-beta to RanBP2/Nup358 filaments is essential for protein import and cell viability. J Cell Biol 194(4):597–612. https://doi.org/10.1083/jcb.201102018
31. Walde S, Thakar K, Hutten S, Spillner C, Nath A, Rothbauer U, Wiemann S, Kehlenbach RH (2012) The nucleoporin Nup358/RanBP2 promotes nuclear import in a cargo- and transport receptor-specific manner. Traffic 13(2):218–233. https://doi.org/10.1111/j.1600-0854.2011.01302.x
32. Patil H, Saha A, Senda E, Cho KI, Haque M, Yu M, Qiu S, Yoon D, Hao Y, Peachey NS, Ferreira PA (2014) Selective impairment of a subset of Ran-GTP-binding domains of Ran-binding protein 2 (Ranbp2) suffices to recapitulate the degeneration of the retinal pigment epithelium (RPE) triggered by Ranbp2 ablation. J Biol Chem 298:29767–29789. https://doi.org/10.1074/jbc.M114.586834
33. Cho KI, Patil H, Senda E, Wang J, Yi H, Qiu S, Yoon D, Yu M, Orry A, Peachey NS, Ferreira PA (2014) Differential loss of prolyl isomerase or chaperone activity of Ran-binding protein 2 (Ranbp2) unveils distinct physiological roles of its cyclophilin domain in proteostasis. J Biol Chem 289(8):4600–4625. https://doi.org/10.1074/jbc.M113.538215
34. Cho KI, Yoon D, Qiu S, Danziger Z, Grill WM, Wetsel WC, Ferreira PA (2017) Loss of Ranbp2 in motoneurons causes disruption of nucleocytoplasmic and chemokine signaling, proteostasis of hnRNPH3 and Mmp28, and development of amyotrophic lateral sclerosis-like syndromes. Dis Model Mech 10(5):559–579. https://doi.org/10.1242/dmm.027730
35. Mavlyutov TA, Cai Y, Ferreira PA (2002) Identification of RanBP2- and kinesin-mediated transport pathways with restricted neuronal and subcellular localization. Traffic 3(9):630–640
36. Kim HJ, Kim NC, Wang YD, Scarborough EA, Moore J, Diaz Z, MacLea KS, Freibaum B, Li S, Molliex A, Kanagaraj AP, Carter R, Boylan KB, Wojtas AM, Rademakers R, Pinkus JL, Greenberg SA, Trojanowski JQ, Traynor BJ, Smith BN, Topp S, Gkazi AS, Miller J, Shaw CE, Kottlors M, Kirschner J, Pestronk A, Li YR, Ford AF, Gitler AD, Benatar M, King OD, Kimonis VE, Ross ED, Weihl CC, Shorter J, Taylor JP (2013) Mutations in prion-like domains in hnRNPA2B1 and hnRNPA1 cause multisystem proteinopathy and ALS. Nature 495(7442):467–473. https://doi.org/10.1038/nature11922
37. Maruyama H, Morino H, Ito H, Izumi Y, Kato H, Watanabe Y, Kinoshita Y, Kamada M, Nodera H, Suzuki H, Komure O, Matsuura S, Kobatake K, Morimoto N, Abe K, Suzuki N, Aoki M, Kawata A, Hirai T, Kato T, Ogasawara K, Hirano A, Takumi T, Kusaka H, Hagiwara K, Kaji R, Kawakami H (2010) Mutations of optineurin in amyotrophic lateral sclerosis. Nature 465(7295):223–226. https://doi.org/10.1038/nature08971
38. Del Bo R, Tiloca C, Pensato V, Corrado L, Ratti A, Ticozzi N, Corti S, Castellotti B, Mazzini L, Soraru G, Cereda C, D'Alfonso S, Gellera C, Comi GP, Silani V, Consortium S (2011) Novel optineurin mutations in patients with familial and sporadic amyotrophic lateral sclerosis. J Neurol Neurosurg Psychiatry 82(11):1239–1243. https://doi.org/10.1136/jnnp.2011.242313
39. Aung T, Rezaie T, Okada K, Viswanathan AC, Child AH, Brice G, Bhattacharya SS, Lehmann OJ, Sarfarazi M, Hitchings RA (2005) Clinical features and course of patients with glaucoma with the E50K mutation in the optineurin gene. Invest Ophthalmol Vis Sci 46(8):2816–2822. https://doi.org/10.1167/iovs.04-1133
40. Rezaie T, Child A, Hitchings R, Brice G, Miller L, Coca-Prados M, Heon E, Krupin T, Ritch R, Kreutzer D, Crick RP, Sarfarazi M (2002) Adult-onset primary open-angle glaucoma caused by mutations in optineurin. Science 295(5557):1077–1079. https://doi.org/10.1126/science.1066901
41. De Marco N, Buono M, Troise F, Diez-Roux G (2006) Optineurin increases cell survival and translocates to the nucleus in a Rab8-dependent manner upon an apoptotic stimulus. J Biol Chem 281(23):16147–16156. https://doi.org/10.1074/jbc.M601467200
42. Munte TF, Troger MC, Nusser I, Wieringa BM, Johannes S, Matzke M, Dengler R (1998) Alteration of early components of the visual evoked potential in amyotrophic lateral sclerosis. J Neurol 245(4):206–210
43. Ringelstein M, Albrecht P, Sudmeyer M, Harmel J, Muller AK, Keser N, Finis D, Ferrea S, Guthoff R, Schnitzler A, Hartung HP, Methner A, Aktas O (2014) Subtle retinal pathology in amyotrophic lateral sclerosis. Ann Clin Transl Neurol 1(4):290–297. https://doi.org/10.1002/acn3.46
44. Hubers A, Muller HP, Dreyhaupt J, Bohm K, Lauda F, Tumani H, Kassubek J, Ludolph AC, Pinkhardt EH (2016) Retinal involvement in amyotrophic lateral sclerosis: a study with optical coherence tomography and diffusion tensor imaging. J Neural Transm (Vienna) 123(3):281–287. https://doi.org/10.1007/s00702-015-1483-4
45. Simonett JM, Huang R, Siddique N, Farsiu S, Siddique T, Volpe NJ, Fawzi AA (2016) Macular sub-layer thinning and association with pulmonary function tests in amyotrophic lateral sclerosis. Sci Rep 6:29187. https://doi.org/10.1038/srep29187
46. Nijssen J, Comley LH, Hedlund E (2017) Motor neuron vulnerability and resistance in amyotrophic lateral sclerosis. Acta Neuropathol 133(6):863–885. https://doi.org/10.1007/s00401-017-1708-8
47. Young P, Qiu L, Wang D, Zhao S, Gross J, Feng G (2008) Single-neuron labeling with inducible Cre-mediated knockout in transgenic mice. Nat Neurosci 11(6):721–728. https://doi.org/10.1038/nn.2118
48. Cho KI, Haque M, Wang J, Yu M, Hao Y, Qiu S, Pillai IC, Peachey NS, Ferreira PA (2013) Distinct and atypical intrinsic and extrinsic cell death pathways between photoreceptor cell types upon specific ablation of Ranbp2 in cone photoreceptors. PLoS Genet 9(6):e1003555. https://doi.org/10.1371/journal.pgen.1003555
49. Dawlaty MM, Malureanu L, Jeganathan KB, Kao E, Sustmann C, Tahk S, Shuai K, Grosschedl R, van Deursen JM (2008) Resolution of sister centromeres requires RanBP2-mediated SUMOylation of topoisomerase IIalpha. Cell 133(1):103–115
50. Yu M, Sturgill-Short G, Ganapathy P, Tawfik A, Peachey NS, Smith SB (2012) Age-related changes in visual function in cystathionine-beta-synthase mutant mice, a model of hyperhomocysteinemia. Exp Eye Res 96(1):124–131. https://doi.org/10.1016/j.exer.2011.12.011
51. Richards SA, Lounsbury KM, Macara IG (1995) The C terminus of the nuclear RAN/TC4 GTPase stabilizes the GDP-bound state

and mediates interactions with RCC1, RAN-GAP, and HTF9A/RANBP1. J Biol Chem 270(24):14405–14411
52. Chi NC, Adam EJ, Adam SA (1995) Sequence and characterization of cytoplasmic nuclear protein import factor p97. J Cell Biol 130(2):265–274
53. Cho KI, Searle K, Webb M, Yi H, Ferreira PA (2012) Ranbp2 haploinsufficiency mediates distinct cellular and biochemical phenotypes in brain and retinal dopaminergic and glia cells elicited by the Parkinsonian neurotoxin, 1-methyl-4-phenyl-1,2,3,6-tetrahydropyridine (MPTP). Cell Mol Life Sci 69(20):3511–3527. https://doi.org/10.1007/s00018-012-1071-9
54. Cho KI, Yi H, Tserentsoodol N, Searle K, Ferreira PA (2010) Neuroprotection resulting from insufficiency of RANBP2 is associated with the modulation of protein and lipid homeostasis of functionally diverse but linked pathways in response to oxidative stress. Dis Model Mech 3(9–10):595–604. https://doi.org/10.1242/dmm.004648
55. Cho KI, Yi H, Yeh A, Tserentsoodol N, Cuadrado L, Searle K, Hao Y, Ferreira PA (2009) Haploinsufficiency of RanBP2 is neuroprotective against light-elicited and age-dependent degeneration of photoreceptor neurons. Cell Death Differ 16(2):287–297. https://doi.org/10.1038/cdd.2008.153
56. Trapnell C, Roberts A, Goff L, Pertea G, Kim D, Kelley DR, Pimentel H, Salzberg SL, Rinn JL, Pachter L (2012) Differential gene and transcript expression analysis of RNA-seq experiments with TopHat and Cufflinks. Nat Protoc 7(3):562–578. https://doi.org/10.1038/nprot.2012.016
57. Chen L, Hambright WS, Na R, Ran Q (2015) Ablation of the ferroptosis inhibitor glutathione peroxidase 4 in neurons results in rapid motor neuron degeneration and paralysis. J Biol Chem 290(47):28097–28106. https://doi.org/10.1074/jbc.M115.680090
58. Altmann C, Vasic V, Hardt S, Heidler J, Haussler A, Wittig I, Schmidt MHH, Tegeder I (2016) Progranulin promotes peripheral nerve regeneration and reinnervation: role of notch signaling. Mol Neurodegener 11(1):69. https://doi.org/10.1186/s13024-016-0132-1
59. Lebrun-Julien F, Suter U (2015) Combined HDAC1 and HDAC2 depletion promotes retinal ganglion cell survival after injury through reduction of p53 target gene expression. ASN Neuro 7(3):1759091415593066. https://doi.org/10.1177/1759091415593066
60. Peachey NS, Roveri L, Messing A, McCall MA (1997) Functional consequences of oncogene-induced horizontal cell degeneration in the retinas of transgenic mice. Vis Neurosci 14(4):627–632
61. Ridder WH 3rd, Nusinowitz S (2006) The visual evoked potential in the mouse—origins and response characteristics. Vision Res 46(6–7):902–913. https://doi.org/10.1016/j.visres.2005.09.006
62. Barnard AR, Charbel Issa P, Perganta G, Williams PA, Davies VJ, Sekaran S, Votruba M, MacLaren RE (2011) Specific deficits in visual electrophysiology in a mouse model of dominant optic atrophy. Exp Eye Res 93(5):771–777. https://doi.org/10.1016/j.exer.2011.07.004
63. O'Neill JH, Jacobs JM, Gilliatt RW, Baba M (1984) Changes in the compact myelin of single internodes during axonal atrophy. Acta Neuropathol 63(4):313–318
64. Soma S, Shimegi S, Suematsu N, Sato H (2013) Cholinergic modulation of response gain in the rat primary visual cortex. Sci Rep 3:1138. https://doi.org/10.1038/srep01138
65. Kirsh O, Seeler JS, Pichler A, Gast A, Muller S, Miska E, Mathieu M, Harel-Bellan A, Kouzarides T, Melchior F, Dejean A (2002) The SUMO E3 ligase RanBP2 promotes modification of the HDAC4 deacetylase. EMBO J 21(11):2682–2691. https://doi.org/10.1093/emboj/21.11.2682
66. Scognamiglio A, Nebbioso A, Manzo F, Valente S, Mai A, Altucci L (2008) HDAC-class II specific inhibition involves HDAC proteasome-dependent degradation mediated by RANBP2. Biochim Biophys Acta 1783(10):2030–2038. https://doi.org/10.1016/j.bbamcr.2008.07.007
67. Tong Y, Eigler T (2009) Transcriptional targets for pituitary tumor-transforming gene-1. J Mol Endocrinol 43(5):179–185. https://doi.org/10.1677/JME-08-0176
68. Waite M, Wakil SJ (1962) Studies on the mechanism of fatty acid synthesis. XII. Acetyl coenzyme A carboxylase. J Biol Chem 237:2750–2757
69. Brownsey RW, Boone AN, Elliott JE, Kulpa JE, Lee WM (2006) Regulation of acetyl-CoA carboxylase. Biochem Soc Trans 34(Pt 2):223–227. https://doi.org/10.1042/BST20060223
70. Lee J, Walsh MC, Hoehn KL, James DE, Wherry EJ, Choi Y (2014) Regulator of fatty acid metabolism, acetyl coenzyme a carboxylase 1, controls T cell immunity. J Immunol 192(7):3190–3199. https://doi.org/10.4049/jimmunol.1302985
71. Berod L, Friedrich C, Nandan A, Freitag J, Hagemann S, Harmrolfs K, Sandouk A, Hesse C, Castro CN, Bahre H, Tschirner SK, Gorinski N, Gohmert M, Mayer CT, Huehn J, Ponimaskin E, Abraham WR, Muller R, Lochner M, Sparwasser T (2014) De novo fatty acid synthesis controls the fate between regulatory T and T helper 17 cells. Nat Med 20(11):1327–1333. https://doi.org/10.1038/nm.3704
72. Dombrowski Y, O'Hagan T, Dittmer M, Penalva R, Mayoral SR, Bankhead P, Fleville S, Eleftheriadis G, Zhao C, Naughton M, Hassan R, Moffat J, Falconer J, Boyd A, Hamilton P, Allen IV, Kissenpfennig A, Moynagh PN, Evergren E, Perbal B, Williams AC, Ingram RJ, Chan JR, Franklin RJM, Fitzgerald DC (2017) Regulatory T cells promote myelin regeneration in the central nervous system. Nat Neurosci 20(5):674–680. https://doi.org/10.1038/nn.4528
73. Kettenmann H, Hanisch UK, Noda M, Verkhratsky A (2011) Physiology of microglia. Physiol Rev 91(2):461–553. https://doi.org/10.1152/physrev.00011.2010
74. Prinz M, Priller J (2014) Microglia and brain macrophages in the molecular age: from origin to neuropsychiatric disease. Nat Rev Neurosci 15(5):300–312. https://doi.org/10.1038/nrn3722
75. Zhao L, Zabel MK, Wang X, Ma W, Shah P, Fariss RN, Qian H, Parkhurst CN, Gan WB, Wong WT (2015) Microglial phagocytosis of living photoreceptors contributes to inherited retinal degeneration. EMBO Mol Med 7(9):1179–1197. https://doi.org/10.15252/emmm.201505298
76. Manicone AM, Birkland TP, Lin M, Betsuyaku T, van Rooijen N, Lohi J, Keski-Oja J, Wang Y, Skerrett SJ, Parks WC (2009) Epilysin (MMP-28) restrains early macrophage recruitment in Pseudomonas aeruginosa pneumonia. J Immunol 182(6):3866–3876. https://doi.org/10.4049/jimmunol.0713949
77. Gharib SA, Johnston LK, Huizar I, Birkland TP, Hanson J, Wang Y, Parks WC, Manicone AM (2014) MMP28 promotes macrophage polarization toward M2 cells and augments pulmonary fibrosis. J Leukoc Biol 95(1):9–18. https://doi.org/10.1189/jlb.1112587
78. Long ME, Gong KQ, Volk JS, Eddy WE, Chang MY, Frevert CW, Altemeier WA, Gale M Jr, Liles WC, Manicone AM (2018) Matrix metalloproteinase 28 is regulated by TRIF- and type I IFN-dependent signaling in macrophages. Innate Immun 24(6):357–365. https://doi.org/10.1177/1753425918791024
79. Werner SR, Dotzlaf JE, Smith RC (2008) MMP-28 as a regulator of myelination. BMC Neurosci 9:83. https://doi.org/10.1186/1471-2202-9-83
80. Smith DH (2009) Stretch growth of integrated axon tracts: extremes and exploitations. Prog Neurobiol 89(3):231–239. https://doi.org/10.1016/j.pneurobio.2009.07.006

81. Kaneb HM, Folkmann AW, Belzil VV, Jao LE, Leblond CS, Girard SL, Daoud H, Noreau A, Rochefort D, Hince P, Szuto A, Levert A, Vidal S, Andre-Guimont C, Camu W, Bouchard JP, Dupre N, Rouleau GA, Wente SR, Dion PA (2015) Deleterious mutations in the essential mRNA metabolism factor, hGle1, in amyotrophic lateral sclerosis. Hum Mol Genet 24(5):1363–1373. https://doi.org/10.1093/hmg/ddu545
82. Patil H, Cho KI, Lee J, Yang Y, Orry A, Ferreira PA (2013) Kinesin-1 and mitochondrial motility control by discrimination of structurally equivalent but distinct subdomains in Ran-GTP-binding domains of Ran-binding protein 2. Open Biol 3(3):120183. https://doi.org/10.1098/rsob.120183
83. Cho KI, Yi H, Desai R, Hand AR, Haas AL, Ferreira PA (2009) RANBP2 is an allosteric activator of the conventional kinesin-1 motor protein, KIF5B, in a minimal cell-free system. EMBO Rep 10(5):480–486. https://doi.org/10.1038/embor.2009.29
84. Cho KI, Cai Y, Yi H, Yeh A, Aslanukov A, Ferreira PA (2007) Association of the kinesin-binding domain of RanBP2 to KIF5B and KIF5C determines mitochondria localization and function. Traffic 8:1722–1735
85. Cai Y, Singh BB, Aslanukov A, Zhao H, Ferreira PA (2001) The docking of kinesins, KIF5B and KIF5C, to Ran-binding protein 2 (RanBP2) is mediated via a novel RanBP2 domain. J Biol Chem 276(45):41594–41602
86. Yoshikawa F, Sato Y, Tohyama K, Akagi T, Furuse T, Sadakata T, Tanaka M, Shinoda Y, Hashikawa T, Itohara S, Sano Y, Ghandour MS, Wakana S, Furuichi T (2016) Mammalian-specific central myelin protein opalin is redundant for normal myelination: structural and behavioral assessments. PLoS One 11(11):e0166732. https://doi.org/10.1371/journal.pone.0166732
87. Parisi V, Manni G, Centofanti M, Gandolfi SA, Olzi D, Bucci MG (2001) Correlation between optical coherence tomography, pattern electroretinogram, and visual evoked potentials in open-angle glaucoma patients. Ophthalmology 108(5):905–912
88. Parisi V (2001) Impaired visual function in glaucoma. Clin Neurophysiol 112(2):351–358
89. Regan D, Milner BA, Heron JR (1976) Delayed visual perception and delayed visual evoked potentials in the spinal form of multiple sclerosis and in retrobulbar neuritis. Brain 99(1):43–66
90. Holder GE (2004) Electrophysiological assessment of optic nerve disease. Eye (Lond) 18(11):1133–1143. https://doi.org/10.1038/sj.eye.6701573
91. Holder GE, Gale RP, Acheson JF, Robson AG (2009) Electrodiagnostic assessment in optic nerve disease. Curr Opin Neurol 22(1):3–10. https://doi.org/10.1097/WCO.0b013e328320264c
92. Chiu IM, Morimoto ET, Goodarzi H, Liao JT, O'Keeffe S, Phatnani HP, Muratet M, Carroll MC, Levy S, Tavazoie S, Myers RM, Maniatis T (2013) A neurodegeneration-specific gene-expression signature of acutely isolated microglia from an amyotrophic lateral sclerosis mouse model. Cell Rep 4(2):385–401. https://doi.org/10.1016/j.celrep.2013.06.018
93. Kapeli K, Pratt GA, Vu AQ, Hutt KR, Martinez FJ, Sundararaman B, Batra R, Freese P, Lambert NJ, Huelga SC, Chun SJ, Liang TY, Chang J, Donohue JP, Shiue L, Zhang J, Zhu H, Cambi F, Kasarskis E, Hoon S, Ares M Jr, Burge CB, Ravits J, Rigo F, Yeo GW (2016) Distinct and shared functions of ALS-associated proteins TDP-43, FUS and TAF15 revealed by multisystem analyses. Nat Commun 7:12143. https://doi.org/10.1038/ncomms12143
94. Lagier-Tourenne C, Polymenidou M, Hutt KR, Vu AQ, Baughn M, Huelga SC, Clutario KM, Ling SC, Liang TY, Mazur C, Wancewicz E, Kim AS, Watt A, Freier S, Hicks GG, Donohue JP, Shiue L, Bennett CF, Ravits J, Cleveland DW, Yeo GW (2012) Divergent roles of ALS-linked proteins FUS/TLS and TDP-43 intersect in processing long pre-mRNAs. Nat Neurosci 15(11):1488–1497. https://doi.org/10.1038/nn.3230
95. Polymenidou M, Lagier-Tourenne C, Hutt KR, Huelga SC, Moran J, Liang TY, Ling SC, Sun E, Wancewicz E, Mazur C, Kordasiewicz H, Sedaghat Y, Donohue JP, Shiue L, Bennett CF, Yeo GW, Cleveland DW (2011) Long pre-mRNA depletion and RNA missplicing contribute to neuronal vulnerability from loss of TDP-43. Nat Neurosci 14(4):459–468. https://doi.org/10.1038/nn.2779
96. Martinez FJ, Pratt GA, Van Nostrand EL, Batra R, Huelga SC, Kapeli K, Freese P, Chun SJ, Ling K, Gelboin-Burkhart C, Fijany L, Wang HC, Nussbacher JK, Broski SM, Kim HJ, Lardelli R, Sundararaman B, Donohue JP, Javaherian A, Lykke-Andersen J, Finkbeiner S, Bennett CF, Ares M Jr, Burge CB, Taylor JP, Rigo F, Yeo GW (2016) Protein-RNA networks regulated by normal and ALS-associated mutant HNRNPA2B1 in the nervous system. Neuron 92(4):780–795. https://doi.org/10.1016/j.neuron.2016.09.050
97. Rotem N, Magen I, Ionescu A, Gershoni-Emek N, Altman T, Costa CJ, Gradus T, Pasmanik-Chor M, Willis DE, Ben-Dov IZ, Hornstein E, Perlson E (2017) ALS along the axons—expression of coding and noncoding RNA differs in axons of ALS models. Sci Rep 7:44500. https://doi.org/10.1038/srep44500
98. Brockington A, Ning K, Heath PR, Wood E, Kirby J, Fusi N, Lawrence N, Wharton SB, Ince PG, Shaw PJ (2013) Unravelling the enigma of selective vulnerability in neurodegeneration: motor neurons resistant to degeneration in ALS show distinct gene expression characteristics and decreased susceptibility to excitotoxicity. Acta Neuropathol 125(1):95–109. https://doi.org/10.1007/s00401-012-1058-5
99. Stolt CC, Wegner M (2016) Schwann cells and their transcriptional network: evolution of key regulators of peripheral myelination. Brain Res 1641(Pt A):101–110. https://doi.org/10.1016/j.brainres.2015.09.025
100. Yoshikawa F, Sato Y, Tohyama K, Akagi T, Hashikawa T, Nagakura-Takagi Y, Sekine Y, Morita N, Baba H, Suzuki Y, Sugano S, Sato A, Furuichi T (2008) Opalin, a transmembrane sialylglycoprotein located in the central nervous system myelin paranodal loop membrane. J Biol Chem 283(30):20830–20840. https://doi.org/10.1074/jbc.M801314200
101. Cahoy JD, Emery B, Kaushal A, Foo LC, Zamanian JL, Christopherson KS, Xing Y, Lubischer JL, Krieg PA, Krupenko SA, Thompson WJ, Barres BA (2008) A transcriptome database for astrocytes, neurons, and oligodendrocytes: a new resource for understanding brain development and function. J Neurosci 28(1):264–278. https://doi.org/10.1523/JNEUROSCI.4178-07.2008
102. Milanesi E, Bonvicini C, Alberici A, Pilotto A, Cattane N, Premi E, Gazzina S, Archetti S, Gasparotti R, Cancelli V, Gennarelli M, Padovani A, Borroni B (2013) Molecular signature of disease onset in granulin mutation carriers: a gene expression analysis study. Neurobiol Aging 34(7):1837–1845. https://doi.org/10.1016/j.neurobiolaging.2012.11.016
103. de Vet EC, Newland SA, Lyons PA, Aguado B, Campbell RD (2005) The cell surface receptor G6b, a member of the immunoglobulin superfamily, binds heparin. FEBS Lett 579(11):2355–2358. https://doi.org/10.1016/j.febslet.2005.03.032
104. Currie E, Schulze A, Zechner R, Walther TC, Farese RV Jr (2013) Cellular fatty acid metabolism and cancer. Cell Metab 18(2):153–161. https://doi.org/10.1016/j.cmet.2013.05.017
105. White DT, Sengupta S, Saxena MT, Xu Q, Hanes J, Ding D, Ji H, Mumm JS (2017) Immunomodulation-accelerated neuronal regeneration following selective rod photoreceptor cell ablation in the zebrafish retina. Proc Natl Acad Sci USA 114(18):E3719–E3728. https://doi.org/10.1073/pnas.1617721114

106. Zhang Y, Zhao L, Wang X, Ma W, Lazere A, Qian HH, Zhang J, Abu-Asab M, Fariss RN, Roger JE, Wong WT (2018) Repopulating retinal microglia restore endogenous organization and function under CX3CL1-CX3CR1 regulation. Sci Adv 4(3):eaap8492. https://doi.org/10.1126/sciadv.aap8492
107. Xu H, Chen M, Mayer EJ, Forrester JV, Dick AD (2007) Turnover of resident retinal microglia in the normal adult mouse. Glia 55(11):1189–1198. https://doi.org/10.1002/glia.20535
108. Muther PS, Semkova I, Schmidt K, Abari E, Kuebbeler M, Beyer M, Abken H, Meyer KL, Kociok N, Joussen AM (2010) Conditions of retinal glial and inflammatory cell activation after irradiation in a GFP-chimeric mouse model. Invest Ophthalmol Vis Sci 51(9):4831–4839. https://doi.org/10.1167/iovs.09-4923
109. Kaplan A, Spiller KJ, Towne C, Kanning KC, Choe GT, Geber A, Akay T, Aebischer P, Henderson CE (2014) Neuronal matrix metalloproteinase-9 is a determinant of selective neurodegeneration. Neuron 81(2):333–348. https://doi.org/10.1016/j.neuron.2013.12.009
110. Kiaei M, Kipiani K, Calingasan NY, Wille E, Chen J, Heissig B, Rafii S, Lorenzl S, Beal MF (2007) Matrix metalloproteinase-9 regulates TNF-alpha and FasL expression in neuronal, glial cells and its absence extends life in a transgenic mouse model of amyotrophic lateral sclerosis. Exp Neurol 205(1):74–81. https://doi.org/10.1016/j.expneurol.2007.01.036
111. Manicone AM, Gharib SA, Gong KQ, Eddy WE, Long ME, Frevert CW, Altemeier WA, Parks WC, Houghton AM (2017) Matrix metalloproteinase-28 is a key contributor to emphysema pathogenesis. Am J Pathol 187(6):1288–1300. https://doi.org/10.1016/j.ajpath.2017.02.008
112. Everts B, Amiel E, Huang SC, Smith AM, Chang CH, Lam WY, Redmann V, Freitas TC, Blagih J, van der Windt GJ, Artyomov MN, Jones RG, Pearce EL, Pearce EJ (2014) TLR-driven early glycolytic reprogramming via the kinases TBK1-IKKvarepsilon supports the anabolic demands of dendritic cell activation. Nat Immunol 15(4):323–332. https://doi.org/10.1038/ni.2833
113. Wu Y, Prystowsky MB, Orlofsky A (1999) Sustained high-level production of murine chemokine C10 during chronic inflammation. Cytokine 11(7):523–530. https://doi.org/10.1006/cyto.1998.0436
114. Asensio VC, Lassmann S, Pagenstecher A, Steffensen SC, Henriksen SJ, Campbell IL (1999) C10 is a novel chemokine expressed in experimental inflammatory demyelinating disorders that promotes recruitment of macrophages to the central nervous system. Am J Pathol 154(4):1181–1191. https://doi.org/10.1016/S0002-9440(10)65370-9
115. Kanno M, Suzuki S, Fujiwara T, Yokoyama A, Sakamoto A, Takahashi H, Imai Y, Tanaka J (2005) Functional expression of CCL6 by rat microglia: a possible role of CCL6 in cell-cell communication. J Neuroimmunol 167(1–2):72–80. https://doi.org/10.1016/j.jneuroim.2005.06.028
116. Nakajima H, Koizumi K (2014) Family with sequence similarity 107: a family of stress responsive small proteins with diverse functions in cancer and the nervous system (Review). Biomed Rep 2(3):321–325. https://doi.org/10.3892/br.2014.243
117. Le PU, Angers-Loustau A, de Oliveira RM, Ajlan A, Brassard CL, Dudley A, Brent H, Siu V, Trinh G, Molenkamp G, Wang J, Seyed Sadr M, Bedell B, Del Maestro RF, Petrecca K (2010) DRR drives brain cancer invasion by regulating cytoskeletal-focal adhesion dynamics. Oncogene 29(33):4636–4647. https://doi.org/10.1038/onc.2010.216
118. Moreno-Mateos MA, Espina AG, Torres B, Gamez del Estal MM, Romero-Franco A, Rios RM, Pintor-Toro JA (2011) PTTG1/securin modulates microtubule nucleation and cell migration. Mol Biol Cell 22(22):4302–4311. https://doi.org/10.1091/mbc.E10-10-0838
119. Rizzo F, Riboldi G, Salani S, Nizzardo M, Simone C, Corti S, Hedlund E (2014) Cellular therapy to target neuroinflammation in amyotrophic lateral sclerosis. Cell Mol Life Sci 71(6):999–1015. https://doi.org/10.1007/s00018-013-1480-4
120. O'Rourke JG, Bogdanik L, Yanez A, Lall D, Wolf AJ, Muhammad AK, Ho R, Carmona S, Vit JP, Zarrow J, Kim KJ, Bell S, Harms MB, Miller TM, Dangler CA, Underhill DM, Goodridge HS, Lutz CM, Baloh RH (2016) C9orf72 is required for proper macrophage and microglial function in mice. Science 351(6279):1324–1329. https://doi.org/10.1126/science.aaf1064